Blockade of associative spine enlargement impairs awake cortical function

Siqi Zhou[1,2†], Takeshi Sawada[1,2†], Tomoki Arima[1-3], Sadam Khan Panezai[1,2], Masanari Ohtsuka[1,2], Hitoshi Okazaki[1-3], Shunki Takaramoto[1,2], Shin-Ichiro Terada[1,3], Masashi Kondo[1,3], Takayuki Hashimoto[1,3], Kenichi Ohki[1,3], Masanori Matsuzaki[1,3,4,5], Sho Yagishita[1,2] & Haruo Kasai[1,2]*

[1]International Research Center for Neurointelligence (WPI-IRCN), UTIAS, The University of Tokyo; Bunkyo-ku, Tokyo 113-0033, Japan.

[2]Laboratory of Structural Physiology, Center for Disease Biology and Integrative Medicine, Faculty of Medicine, The University of Tokyo; Bunkyo-ku, Tokyo 113-0033, Japan.

[3]Department of Physiology, Graduate School of Medicine, The University of Tokyo; Bunkyo-ku, Tokyo 113-0033, Japan.

[4]Brain Functional Dynamics Collaboration Laboratory, RIKEN Center for Brain Science, Saitama, 351-0198, Japan.

[5]Department of Biological Sciences, Graduate School of Science, The University of Tokyo, Tokyo, 113-0033, Japan.

*Corresponding author. hkasai@m.u-tokyo.ac.jp (H.K.)

[†]These authors contributed equally to this work.

Abstract

Awake cortical processing shows distinctive patterns in electroencephalography (EEG), electromyography (EMG), and locomotor activity, reflecting coordinated neural dynamics driven by action potentials and synaptic transmission across wide cortical territories. Although memory processes are consistently engaged during these states, the causal role of associative synaptic plasticity—specifically dendritic-spine enlargement—in sustaining cortical processing and wakefulness has remained unknown, owing to the absence of tools that can selectively abolish spine enlargement in vivo. Here we show that a Rac1-GAP-based variant of Synaptic Chemogenetics (SYNCit-C, SynC), selectively and reversibly abolishes spine enlargement after administration of an A/C heterodimeriser, while preserving cellular excitability and NMDA-receptor function. Visual cortical responses were preserved, whereas motor learning in the motor cortex was impaired. With broad frontoparietal expression of SynC, A/C administration induced reversible deficits in goal-directed behaviours, including laser-dot chasing and feeding initiation. It also induced intermittent State-C, a state outside canonical wake and sleep, marked by behavioural arrest with reduced γ-power and a muted rise in slow δ-waves during these episodes. SynC–A/C preserved firing and Ca^{2+} rates but reduced pairwise spike correlations. All effects reversed within ~1 h. These findings provide direct causal evidence that associative dendritic-spine enlargement sustains cortical processing and wakefulness.

Introduction

Wakefulness is essential for animals to flexibly process environmental stimuli, enabling sensory integration, motor control and task-relevant cortical processing. These processes depend on coordinated cortical network dynamics integrating both working- and long-term-memory mechanisms[1-5]. Despite the established role of memory mechanisms in these processes, the specific contribution of associative synaptic plasticity—such as dendritic-spine enlargement—to awake cortical function remains unclear. NMDA receptor antagonists such as ketamine disrupt associative plasticity, impair memory formation and cognitive performance[6], and induce anaesthesia[7], yet also broadly suppress NMDA-receptor-mediated synaptic currents. Thus, the specific role of plasticity mechanisms—distinct from general synaptic transmission—in sustaining wakefulness and cognitive processing remains elusive.

Most excitatory synapses reside on actin-rich dendritic spines. During coincident pre- and postsynaptic activity, dendritic spines undergo a long-lasting increase in head volume ("spine enlargement")[8-10]. Spine enlargement can strengthen synaptic connections via two complementary routes: (i) by increasing postsynaptic glutamate responsiveness through AMPA-receptor recruitment/stabilisation—often operationalised as long-term potentiation (LTP)[9,11-13]; and (ii) a trans-synaptic mechanotransduction route has been proposed, whereby actin-driven spine expansion engages adhesion complexes and influence presynaptic release[10,13,14]. The onset of such associative plasticity occurs within seconds[15,16], yet direct sub-minute in vivo measurements during behaviour remain technically challenging. Here, "spine

74 enlargement" refers to a sustained increase in spine-head volume, representing the
75 morphological correlate of associative plasticity.
76 We developed SYNCit-C (SynC), a chemogenetic variant of SYNCit-K (SynK)[17],
77 that selectively and transiently abolishes dendritic-spine enlargement after
78 administration of the A/C heterodimeriser, without affecting basal synaptic
79 transmission, NMDA-receptor-mediated slow EPSCs, or membrane properties.
80 Knockout mice lacking CaMKII and other kinases fail to block the transient
81 component[18], whereas SynC abolishes spine enlargement while preserving NMDA-
82 receptor function. To test whether spine enlargement contributes to task-relevant
83 processing, we expressed SynC broadly across the frontoparietal cortex[19]. A/C
84 administration induced severe deficits in awake behaviours and produced an
85 intermittent non-wakeful state (State-C), distinct from slow-wave sleep (SWS) and
86 marked by behavioural arrest with a characteristic EEG pattern. These findings indicate
87 that dendritic-spine enlargement is not only engaged in learning and memory but is also
88 required to sustain coordinated cortical processing and wakefulness.
89

90 Selective inhibition of spine enlargement by SynC

91 We designed SynC to block activity-dependent spine enlargement, building on the
92 previously reported SynK system, which uses a rapamycin derivative (A/C)-induced
93 heterodimerisation of FKBP (FK506-binding protein) and FRB (the FKBP12–
94 rapamycin binding domain of mTOR) by A/C (Fig. 1a)[17]. Because SynK implicated
95 Rac1 activation by Rac1-GEFs in spine enlargement (Fig. 1b), we generated SynC in
96 which both components were expressed from the CaMKII(0.4) promoter: a PSD-
97 anchored PSDΔ1,2–FRB and a cytosolic FKBP–Rac1-GAP (the GAP domain of α1-

98 chimaerin) to inactivate Rac1 by GTP hydrolysis (Fig. 1b) PSDΔ1,2–FRB–mVenus
99 localised selectively to postsynaptic densities and was absent from axons (Extended
100 Data Fig. 1a,b). Application of A/C rapidly recruited the FKBP fusion from dendritic
101 shafts into spines (Fig. 1e–g, Extended Data Fig.1c), and abolished spine enlargement
102 evoked by a chemical LTP (cLTP) protocol (Fig. 1c–h), an effect not observed with the
103 GAP-dead mutant SynC-dGAP (Fig. 1d,f–h; Extended Data Fig. 1c). These results are
104 consistent with rapid Rac1-GAP catalysis being sufficient to suppress Rac1-dependent
105 spine enlargement under these conditions[20,21].

106 We assessed SynC in hippocampal slice cultures[8] by co-expressing CaMKII(0.4)-
107 Cre with floxed SynC and mScarlet, enabling targeted whole-cell recordings from
108 mScarlet-positive neurons (Extended Data Fig. 2a,b). In control cells, two-photon
109 glutamate uncaging in 0 Mg^{2+} ACSF robustly induced spine enlargement; with SynC,
110 A/C abolished this response—including the transient phase reported to resist many
111 other perturbations[10]—whereas the GAP-dead SynC-dGAP had no effect (Extended
112 Data Fig. 2b). Basal excitatory and inhibitory synaptic transmission and intrinsic
113 membrane properties were unchanged, and, notably, NMDA receptor–mediated slow
114 EPSCs were unaffected (Extended Data Fig. 2c–g).

115 For most subsequent experiments, we used a bicistronic plasmid in which the
116 FRB and FKBP modules of SynC were co-expressed via an internal ribosome entry site
117 (IRES), enabling single-vector AAV-mediated delivery for in vivo use (Fig. 1i)[17]. We
118 further characterized this construct in dissociated culture, and found that SynC activity
119 was transient following A/C: at ~0.3 $\mu g\ mL^{-1}$ plasmid DNA, A/C nearly abolished
120 spine enlargement, but the effect dissipated within ~1 h (Fig. 1j,k, Extended Data
121 Fig. 1d,e), even though FKBP–mVenus fluorescence persisted (Extended Data Fig. 1e).

122 This rapid loss of efficacy is consistent with inactivation of the tethered Rac1-GAP[22]
123 rather than diminished expression, and it enables reversible induction of cortical deficits
124 in vivo (see Fig. 4g). SynC neither altered NMDA-evoked spine shrinkage (Extended
125 Data Fig. 1f), nor baseline spine morphology and intrinsic spine volume dynamics[17,23]
126 (Extended Data Fig. 1g). For in vivo AAV delivery, mVenus was replaced by an HA
127 tag, reducing the expression cassette to 4.5 kb (Fig. 2a).
128

129 Local SynC expression in primary visual and motor cortices

130 We tested whether SynC perturbs basic response properties in primary visual cortex
131 (V1). SynC was delivered to Thy1–GCaMP6s transgenic mice by AAV
132 (1.2×10^{13} gc mL^{-1}; 1 μL; Extended Data Fig. 3a,b). Four weeks later, we recorded
133 responses to grating stimuli from hundreds of neurons. A/C (2 mg mL^{-1}) was then
134 intraperitoneally (i.p.) administered under light anaesthesia (Methods). Retinotopy,
135 orientation selectivity and neuronal firing rates were unchanged following A/C in SynC-
136 expressing mice (SynC@V1) (Extended Data Fig. 3c–k). Thus, acute SynC activation
137 did not impair basic visual processing in V1, indicating that intrinsic membrane
138 properties and synaptic transmission remained intact in vivo, consistent with in vitro
139 controls.
140 We next examined motor learning in primary motor cortex (M1). SynC was
141 bilaterally delivered to the forelimb representations by AAV (Fig. 2a), and rotarod
142 training was performed 4 weeks later. Within 30 min of i.p. A/C, translocation of HA–
143 FKBP–Rac1-GAP to dendritic spines was detected in fixed SynC@M1 tissue (Fig. 2b).
144 Each training session lasted 30 min; in controls, performance improved rapidly within
145 the first 20 min and typically plateaued by ~30 min and maintained and consolidated in

146 the next day (Fig. 2c,d). In SynC@M1 mice, A/C abolished rotarod learning, whereas
147 A/C alone or A/C in SynC-dGAP mice left learning intact (Fig. 2d). These data indicate
148 that long-term motor learning in this task requires Rac1-dependent spine enlargement,
149 which SynC–A/C blocks via inhibition of Rac1 at spines.
150

151 **SynC expression across frontoparietal cortex**

152 To test the impact of spine enlargement on goal-directed behaviour[19], we bilaterally
153 transduced SynC using AAV at 1.2×10^{13} gc mL^{-1} (4 µL) in neonatal pups (P1) under
154 hypothermic (ice) anaesthesia, targeting a site between S1 and M2 in the sagittal plane
155 (AP 0–1 mm; ML 1 mm) (Fig. 3a; Extended Data Fig. 4a,b). Injection at P1 ensured
156 extensive cortical distribution[24]. At 6–12 weeks post-injection, histology showed broad
157 expression spanning from prefrontal cortex (M2) to the posterior parietal cortex (PPC),
158 with minimal subcortical labelling except for minor dorsal striatal spillover (Extended
159 Data Fig. 4c). Across transduced areas, 20–80% of $NeuN^+$ neurons expressed SynC,
160 varying by cortical region (Extended Data Fig. 4c) No gross or cytoarchitectural
161 abnormalities were detected (Fig. 3a) and SynC@FPC mice displayed normal motor
162 performance in the rotarod task comparable to WT mice (Fig. 2e). The cortical area of
163 middle sagittal sections were slightly smaller in SynC@FPC (mean ± s.e.m.= 7.9 ± 0.40
164 mm^2, for thickness 2.5 ± 0.097 mm, n = 14) compared to SynC-dGAP@FPC (8.9 ± 0.49
165 mm^2, thickness 2.75 ± 0.087, n = 10), but these differences were not significant.
166 Expression was most prominent in layer V neurons, moderate in layer II,III, and nearly
167 absent in layer VI, consistent with the CaMKII promoter (Fig. 3a; Extended Data
168 Fig. 4d). PSDΔ1,2–FRB–mVenus was largely restricted to dendritic spines, with no

169 clear labelling observed in dendritic shaft, somatic cytosol, nucleus or axon in vivo
170 (Extended Data Fig. 4e).
171 Following i.p. A/C, locomotor speed decreased similarly in SynC@FPC and
172 SynC@M1 mice, but SynC@FPC mice exhibited a significantly greater reduction in
173 centre exploration relative to SynC@M1 (Fig. 3b). Behavioural assays (Fig. 3b–d) were
174 analysed in animals subsequently confirmed to have sufficient cortical SynC expression
175 (see criteria in Fig. 4b). We next probed innate, goal-directed behaviours. In a laser-dot
176 chasing assay (Methods), SynC@FPC mice pursued the moving or stationary spot in
177 80% of trials before A/C (n = 26 mice), but this was dramatically reduced (15%) after
178 A/C injection (Fig. 3c; Extended Data Movies 1–4). These behavioural deficits were not
179 observed in control SynC-dGAP@FPC mice (n = 16, Fig. 3b,c). In a food-pellet task,
180 mice without A/C initiated feeding within ~30 s, whereas after A/C, SynC@FPC mice
181 required ~150 s despite frequent encounters with the pellet (Fig. 3d; Extended Data
182 Movies 5–7). These delays indicate profound deficits in cortical processes required to
183 initiate goal-directed actions, while basic motor output and consummatory behaviour
184 remained intact. The overall phenotype is reminiscent of classical observations in
185 decorticated dogs, which stand, walk, and chew food placed in the mouth yet fail to
186 initiate feeding independently[1,25]. Because precise onset/resolution requires stable
187 wakefulness, we quantified the time course in a separate dark-phase cohort (see
188 Fig. 4g).
189

190 **Intermittence of State-C and Interm-C**

191 Following i.p. injection of A/C in the open-field arena, 41 of 57 SynC@FPC mice
192 exhibited intermittent behavioural arrests beginning 3–15 min post-injection,

193 cumulatively occupying approximately 31.2 % (± 3.8%, n = 29) of the first hour
194 (Fig. 4a). Arrest episodes frequently occurred during standing at the end of running
195 bouts ("standing"), while navigating corners ("corner"), or during grooming
196 ("grooming") (Extended Data Fig. 5; Movies 8-11). During these episodes, animals
197 remained motionless in an awake-like posture with eyes open, head elevated, and tail
198 extended, typically fully standing or partially seated ("corner"), except for occasional
199 minor postural shifting in the "corner" state (Extended Data Fig. 5b; Movie 12; see
200 below). To relate phenotype to SynC expression levels, we performed whole-brain
201 histology in 21 mice; the five mice without State-C showed <20% neuronal expression,
202 while State-C reliably appeared when expression exceeded this threshold (Fig. 4b;
203 Extended Data Fig. 4c). Since the occurrence of State-C reliably indicated sufficient
204 SynC expression, behavioural assays shown in Fig. 3d–d were analysed specifically in
205 mice exhibiting State-C to ensure phenotype-expression consistency. State-C required
206 Rac1-GAP activity in neocortical dendritic spines, as A/C did not induce State-C in
207 SynC-dGAP@FPC mice with histologically confirmed expression (Fig. 4e, Extended
208 Data Fig. 4b,c). Expression of the FKBP–Rac1-GAP–HA component alone also failed
209 to induce State-C (Fig. 4e), arguing against potential confounding effects mediated by
210 endogenous mTOR activation. The local SynC expression to M1 never caused State-C
211 (Fig. 4e).
212 Electrophysiologically, State-C was characterized by reduced EMG tone and
213 suppressed γ-band power, reminiscent of SWS (Fig. 4c,d; Extended Data Fig. 6a–c).
214 Unlike typical SWS, State-C did not exhibit a robust increase in slow-wave (δ-band)
215 power (Fig. 4c,d; Extended Data Fig. 6c). This contrasts sharply with the robust slow-
216 wave increase previously reported for SynK, which promotes spine enlargement in

217 frontal cortex[17]. Isolated sleep spindles, a hallmark of stage-2 sleep, were frequently
218 observed in State-C but rarely seen in matched control recordings (Extended Data
219 Fig. 6a)[26]. Spike-and-wave discharges characteristic of absence seizures[27] were not
220 observed (Extended Data Movie 8). Pupils constricted (miosis), heart rate modestly
221 decreased, and respiration remained unchanged, similar to autonomic patterns observed
222 in SWS (Fig. 4f). However, this overall autonomic/motor signature clearly differed from
223 arrest induced by fear or brainstem stimulation[28]. REM sleep (θ-band dominance with
224 low EMG; Extended Data Fig. 6a) was not observed during State-C, clearly
225 distinguishing it from narcolepsy[29]. To aid accurate classification and avoid confusion
226 with other behavioural and physiological states, we provide an orientation map clearly
227 distinguishing Interm-C/State-C from sleep, seizure, narcolepsy/cataplexy, catalepsy,
228 and anesthesia (Extended Data Table 1).
229 A/C initially induced a locomotor-active state with impaired goal-directed
230 performance (e.g., reduced chasing or feeding initiation; hereafter 'Interm-C'; Fig. 3),
231 and intermittently caused State-C. EEG γ-band power (30–80 Hz) in Interm-C remained
232 comparable to awake periods recorded from the same mice prior to A/C administration
233 (Awake baseline) (Fig. 4c,d; Extended Data Fig. 6c). The duration of Interm-C bouts
234 followed a heavy-tailed (power-law) distribution, similar to awake bouts in WT mice. In
235 contrast, State-C bout durations were exponentially distributed (Extended Data Fig. 6d).
236 Interm-C and State-C thus alternated finely (Fig. 4d), with State-C episodes often
237 briefly interrupted (0.5–10 s) by short movements ("shifting") that coincided with
238 transient EEG γ-wave activation, especially during "corner" postures (Extended Data
239 Fig. 5b; Movie 12). These alternating State-C and Interm-C dynamics closely resemble

240 sleep–wake transitions and suggest flip-flop-like mechanisms mediated by the
241 ascending reticular activating system (ARAS)[29,30].
242 To examine the time course of State-C and behavioural abnormalities during
243 stable wakefulness, we housed mice on an inverted light–dark cycle and tested them
244 during their nocturnal (active) phase. State-C emerged similarly to tests performed
245 during their normal inactive (light) phase (31% ± 4.6%, n = 49). The onset of State-C
246 and impairments in laser-chasing and food-pellet tasks occurred by ~10 min after A/C
247 administration and resolved by ~60 min (Fig. 4g). This reversibility paralleled the
248 transient SynC–A/C action on spine enlargement observed in dissociated culture
249 (Extended Data Fig. 1i–l). Thus, the transient effects of A/C closely mirrored those
250 observed with low-dose expression in dissociated culture experiments that inhibited
251 cLTP (Fig. 1j,k, Extended Data Fig. 1d,e). Occurrence of State-C, impaired laser-
252 chasing, and delayed feeding initiation resolved in parallel (Fig. 4g), supporting a
253 common mechanism—acute inhibition of spine enlargement. The transient nature of
254 SynC–A/C effects was further confirmed by normal rotarod performance tested one day
255 after training, even when A/C administration shortly after training had induced State-C
256 (Fig. 2e). This indicates that newly acquired motor memories were preserved and
257 successfully consolidated. Moreover, A/C-induced State-C was reproducible three
258 weeks later in 8 out of 9 previously responsive mice (Fig. 4e), demonstrating that
259 transient SynC–A/C action does not induce long-lasting neural dysfunction or tolerance.
260

261 **Transitions between Interm-C and State-C**

262 State-C occurred even during the nocturnal (active) phase, when mice are normally
263 awake (Fig. 4g), and tended to appear similar at night (Fig. 4e,g). This finding suggests

264 that brainstem arousal cannot be fully sustained under conditions of widespread cortical
265 suppression. To examine this mechanism, we performed time-resolved analyses of
266 transitions from Interm-C to State-C. In untreated control mice, transitions toward sleep
267 proceeded gradually, with progressive declines in locomotor velocity, EMG tone, and
268 cortical γ power over 10–60 s, typically as animals settled in a corner and oriented their
269 head toward the centre of the arena (Extended Data Fig. 5d; Movie 13). In contrast,
270 SynC@FPC mice after A/C exhibited abrupt transitions, marked by rapid decreases in
271 locomotor velocity and cortical γ power within ~10 s (Extended Data Fig. 7b,c; Movie
272 14). Averaged, time-locked analyses revealed highly reproducible profiles across
273 animals (Extended Data Fig. 7). Despite variability in awake behaviour, this stereotyped
274 pattern supports our working hypothesis that cortical associative activity sustains
275 brainstem arousal, buffering against sudden inactivation and allowing gradual descent
276 into sleep-like postures. When cortical control is disrupted, rapid brainstem inactivation
277 ensues, producing immediate behavioural arrest (State-C) even during ongoing
278 movement.

279 Across three goal-directed behavioural assays—open-field centre exploration
280 (motivation), laser-dot chasing (attention/motivation), and feeding initiation
281 (motivation)—SynC–A/C consistently impaired performance. These assays likely
282 engage multiple cognitive processes (e.g., perception, attention, motivation) and were
283 not designed to isolate specific domains; rather, we interpret them collectively as
284 reflecting an integrated capacity for goal-directed cortical processing. Because State-C
285 occurred frequently and Interm-C episodes were temporally fragmented, conventional
286 tasks requiring sustained engagement (e.g., T-maze, novel object recognition) could not
287 be validly performed or reliably interpreted. Region-specific SynC expression using

288 lower viral titres may, in future, mitigate State-C occurrence and reveal circuit-specific
289 dependencies of associative plasticity on goal-directed behaviour. In the present study,
290 our aim was to establish that rapid dendritic-spine enlargement is required for intact
291 goal-directed cortical performance and the stabilisation of wakefulness.
292

293 **Ca^{2+} imaging from primary motor cortex (M1)**

294 We performed two-photon Ca^{2+} imaging in the forelimb area of M1 in head-fixed
295 SynC@FPC mice co-transfected with GCaMP7f while the mice ran on a treadmill (Fig.
296 5a,b). The amplitudes and time courses of Ca^{2+} transients remained unchanged
297 following A/C administration (Fig. 5c, Extended Data Fig. 8a,b), indicating that SynC–
298 A/C did not affect voltage-gated ion channels and NMDA receptor function[31],
299 supporting in vitro and V1 experiments (Extended Data Fig. 2c,g, 3). Mice typically ran
300 at mean velocities of approximately 4.7 ± 1.5 cm s^{-1} (mean ± s.e.m., n = 5 mice) during
301 the Awake and 3.5 ± 1.3 cm s^{-1} during Interm-C. However, during approximately 30%
302 of the recorded time, the mice stopped moving and became immobile (Fig. 5d). When
303 immobile, Awake mice maintained a stable posture with their legs spread to grasp the
304 treadmill, whereas Interm-C mice exhibited more arbitrary and uncontrolled leg
305 positions (Extended Data Movies 15, 16). Although the average degrees of firing
306 correlation during running were similar between Awake and Interm-C states (Fig. 5e),
307 the firing patterns themselves differed notably between these states (Fig. 5f).
308 The immobile phases enabled us to examine cortical firing patterns independently
309 of motion. Importantly, firing rates were not significantly reduced after A/C
310 administration (Fig. 5e), consistent with the preserved γ-band power observed during
311 Interm-C (Extended Data Fig. 6c). Pairwise spike correlations during immobile Interm-

312 C periods were reduced by A/C (Fig. 5f,g). Concurrently, neuronal network
313 dimensionality increased, as indicated by a greater number of principal components
314 explaining 50% of variance (D50) and increased participation ratios (PR; Extended Data
315 Fig. 8c,d). This reduction in correlation accompanied by increased dimensionality
316 suggests weakened functional coupling among M1 neurons, rather than a general
317 suppression of neuronal firing. Interestingly, similar correlation patterns tended to
318 recover 1 h after A/C particularly in immobile phase (Fig. 5f). These findings align with
319 impaired goal-directed behaviour during Interm-C and the inhibition of associative
320 plasticity by SynC. The dissociation between neuronal correlation and firing rates
321 observed here is consistent with previous electrophysiological findings demonstrating
322 perception-related membrane depolarization independently of spike-rate modulation[32].
323 Additionally, when we identified State-C based on EEG and EMG power in treadmill
324 experiments (Fig. 5d), we found that firing rates were reduced to levels comparable to
325 SWS. However, pairwise correlations were decreased and dimensionality increased in
326 State-C—contrary to SWS, in which correlations typically increase and dimensionality
327 decreases due to firing synchrony induced by slow waves (Extended Data Table 2)[33].
328 Such synchrony was notably suppressed in State-C.
329
330

331 Discussion

332 We developed SynC, a chemogenetic tool acutely activated by the A/C heterodimeriser
333 that selectively and reversibly abolishes dendritic-spine enlargement while preserving
334 neuronal excitability—including NMDA-receptor function—and physiological spine

335 dynamics such as shrinkage and actin-driven fluctuations. In vivo, cortical SynC–A/C
336 left early visual responses in V1 intact but impaired long-term motor learning, assessed
337 by rotarod performance. With broad expression across the frontoparietal cortex, SynC–
338 A/C rapidly disrupted goal-directed cortical processing during Interm-C, including
339 open-field exploration, laser-dot chasing and feeding initiation. SynC expression alone
340 produced no detectable baseline effects before A/C administration (Fig. 2e). SynC–A/C
341 showed a rapid onset (~10 min) and reversal (~60 min) of effects in vivo (Fig. 4g),
342 closely matching the in vitro kinetics (Fig. 1k) and consistent with a reversible block of
343 spine enlargement at low SynC expression levels and reproducible effects in vivo.
344 These results confirm the on-target mechanism—an acute blockade of spine
345 enlargement.

346 To verify target specificity, we examined subcellular localisation and genetic
347 controls. The FRB probe localised to the PSD, but not to somata or axons, both in vitro
348 and in vivo. Specificity was confirmed by the GAP-dead genetic control (SynC-dGAP),
349 which preserves FRB/FKBP scaffolding and A/C dimerisation but lacks Rac1-GAP
350 catalysis. It produced no rapid phenotypes, making A/C-only or scaffold-only
351 explanations—including endogenous mTOR activation—unlikely. The rapid, reversible
352 and PSD-restricted phenotype is inconsistent with diffuse or delayed Rac1-linked
353 inhibition, which normally unfolds over longer timescales[20,21] and would be attenuated
354 rather than recruited by a PSD-tethered Rac1-GAP. Two-photon Ca^{2+} imaging showed
355 that during Interm-C, gross spiking and Ca^{2+} rates and γ-power were comparable to
356 Awake, whereas pairwise spike correlation decreased (Fig. 6). In State-C, spiking fell to
357 SWS-like levels, γ-power decreased and δ-power showed a slight rise, accompanied by
358 behavioural arrest and reduced EMG tone. Five converging lines of evidence—(i)

359 functional selectivity (enlargement blocked while excitability and NMDA function are
360 preserved), (ii) rapid and reversible phenotypes, (iii) PSD-restricted localisation of the
361 activated probe, (iv) catalytic specificity shown by the Rac1-GAP-dead mutant, and (v)
362 a state-dependent network signature—together rule out broad cortical inhibition or
363 nonspecific ligand/scaffold-related effects, including unrecognised SynC–A/C species
364 (Extended Data Table 2).

365 Moreover, SynC–A/C reduced the propensity for slow-wave activity (SWA),
366 attenuating the δ-power rise, whereas promoting spine enlargement with SynK–A/C (a
367 Rac1-GEF probe) increased SWA[17]. These opposite effects strongly support the
368 conclusion that SynC primarily acts by blocking spine enlargement. Complementary
369 effects on arousal further suggest a top-down cortical influence on brainstem systems.
370 Both manipulations reduce indices of cortical computation: SynC by blocking plasticity
371 and inducing ensemble decorrelation (expanded dimensionality), and SynK by inducing
372 slow-wave bistability that synchronises up–down transitions and interrupts information
373 exchange. In both cases, cortical contribution to arousal decreases. Such top-down
374 modulation of sleep has been proposed in psychological[34] and physiological
375 frameworks[17,35,36] and is anatomically plausible given frontal-cortex projections to
376 brainstem nuclei[37,38], although the specific targets remain unidentified and beyond the
377 scope of this study.

378 Awake cortical functions represent higher-order processes that integrate sensory
379 input with working and long-term memory to enable decision-making, predictive
380 behaviour and executive control[1,3,39]. James proposed that cognitive acts are in constant
381 flux and that memory is continuously reshaped[1], and rapid neocortical associative
382 plasticity has been reported[3-5]. A recent theoretical model suggests that fast Hebbian

383 plasticity can induce synapse-driven network states or transient attractors underlying
384 working memory[40-42], potentially corresponding to the dynamic correlated activities we
385 observed (Fig. 5d). Consistent with this view, our experiments demonstrate that
386 associative plasticity—specifically spine enlargement—is required for awake cortical
387 function beyond network spiking dynamics[19,29,30]. Although the precise kinetics of
388 cortical associative plasticity remain uncertain, evidence suggests they occur
389 rapidly[2,15,16,43]. Increases in postsynaptic glutamate sensitivity, however, require longer
390 (~2 min)[12,44]. Thus, rapid plasticity may instead be mediated, at least in part, by trans-
391 synaptic mechanical effects of spine enlargement on presynaptic terminals[10,14],
392 consistent with presynaptic expression of associative plasticity previously reported in
393 the neocortex[45-47].
394 Current in vivo imaging method for detecting spine-head enlargement necessarily
395 relies on intensity-based measurements and are constrained by diffraction-limited
396 optical resolution. In the awake cortex, spine imaging is particularly susceptible to
397 motion artefacts and intrinsic spine dynamics (Extended Data Fig. 1g), complicating
398 reliable detection[13,48,49]. Moreover, even subtle (1–2%) coordinated synaptic changes—
399 but not intrinsic dynamics an order of magnitude larger—are considered functionally
400 significant[50], further highlighting the challenge of detection. Artificial, time-locked
401 induction methods for directly visualising SynC's proximal action remain technically
402 demanding and low yield[16,43]. Future advances in direct in vivo imaging will enhance
403 mechanistic understanding, but establishing causal links to behaviour requires targeted
404 perturbation. SynC provides such an approach, enabling behavioural modulation
405 without detectable changes in mean population firing rate.
406

References

1. James, W. *The Principle of Psychology*. (H. Holt, 1890).
2. Erickson, M. A., Maramara, L. A. & Lisman, J. A single brief burst induces GluR1-dependent associative short-term potentiation: a potential mechanism for short-term memory. *J Cogn Neurosci* **22**, 2530–2540 (2010).
3. Jonides, J., Lewis, R. L., Nee, D. E., Lustig, C. A., Berman, M. G. *et al.* The mind and brain of short-term memory. *Annu Rev Psychol* **59**, 193–224 (2008).
4. Brodt, S., Gais, S., Beck, J., Erb, M., Scheffler, K. *et al.* Fast track to the neocortex: A memory engram in the posterior parietal cortex. *Science* **362**, 1045–1048 (2018).
5. Yount, S. T., Li, D. C., Stachowicz, K. M., Seo, E. H., Knight, K. A. *et al.* Parallel neuronal structural plasticity with memory trace formation in the orbitofrontal cortex. *Nature communications* **16**, 8521 (2025).
6. Driesen, N. R., McCarthy, G., Bhagwagar, Z., Bloch, M. H., Calhoun, V. D. *et al.* The impact of NMDA receptor blockade on human working memory-related prefrontal function and connectivity. *Neuropsychopharmacology* **38**, 2613–2622 (2013).
7. Franks, N. P. General anaesthesia: from molecular targets to neuronal pathways of sleep and arousal. *Nature reviews. Neuroscience* **9**, 370–386 (2008).
8. Matsuzaki, M., Honkura, N., Ellis-Davies, G. C. & Kasai, H. Structural basis of long-term potentiation in single dendritic spines. *Nature* **429**, 761–766 (2004).
9. Holtmaat, A. & Svoboda, K. Experience-dependent structural synaptic plasticity in the mammalian brain. *Nature reviews. Neuroscience* **10**, 647–658 (2009).
10. Kasai, H., Ucar, H., Morimoto, Y., Eto, F. & Okazaki, H. Mechanical transmission at spine synapses: Short-term potentiation and working memory. *Curr Opin Neurobiol* **80**,

432 102706 (2023).
433 11. Herring, B. E. & Nicoll, R. A. Long-term potentiation: from CaMKII to AMPA receptor
434 trafficking. *Annu Rev Physiol* **78**, 351–365 (2016).
435 12. Getz, A. M., Ducros, M., Breillat, C., Lampin-Saint-Amaux, A., Daburon, S. *et al.*
436 High-resolution imaging and manipulation of endogenous AMPA receptor surface
437 mobility during synaptic plasticity and learning. *Sci Adv* **8**, eabm5298 (2022).
438 13. Harris, K. M., Kuwajima, M., Flores, J. C. & Zito, K. Synapse-specific structural
439 plasticity that protects and refines local circuits during LTP and LTD. *Philos Trans R*
440 *Soc Lond B Biol Sci* **379**, 20230224 (2024).
441 14. Ucar, H., Watanabe, S., Noguchi, J., Morimoto, Y., Iino, Y. *et al.* Mechanical actions of
442 dendritic-spine enlargement on presynaptic exocytosis. *Nature* **600**, 686–689 (2021).
443 15. Gustafsson, B., Asztely, F., Hanse, E. & Wigstrom, H. Onset Characteristics of Long-
444 Term Potentiation in the Guinea-Pig Hippocampal CA1 Region in Vitro. *Eur J Neurosci*
445 **1**, 382–394 (1989).
446 16. El-Boustani, S., Ip, J. P. K., Breton-Provencher, V., Knott, G. W., Okuno, H. *et al.*
447 Locally coordinated synaptic plasticity of visual cortex neurons in vivo. *Science* **360**,
448 1349–1354 (2018).
449 17. Sawada, T., Iino, Y., Yoshida, K., Okazaki, H., Nomura, S. *et al.* Prefrontal synaptic
450 regulation of homeostatic sleep pressure revealed through synaptic chemogenetics.
451 *Science* **385**, 1459–1465 (2024).
452 18. Incontro, S., Diaz-Alonso, J., Iafrati, J., Vieira, M., Asensio, C. S. *et al.* The
453 CaMKII/NMDA receptor complex controls hippocampal synaptic transmission by
454 kinase-dependent and independent mechanisms. *Nature communications* **9**, 2069
455 (2018).
456 19. International Brain, L., Angelaki, D., Benson, B., Benson, J., Birman, D. *et al.* A brain-
457 wide map of neural activity during complex behaviour. *Nature* **645**, 177–191 (2025).

20. Bosco, E. E., Mulloy, J. C. & Zheng, Y. Rac1 GTPase: a "Rac" of all trades. *Cellular and molecular life sciences : CMLS* **66**, 370–374 (2009).

21. Arimura, N. & Kaibuchi, K. Neuronal polarity: from extracellular signals to intracellular mechanisms. *Nature reviews. Neuroscience* **8**, 194–205 (2007).

22. Griner, E. M., Caino, M. C., Sosa, M. S., Colon-Gonzalez, F., Chalmers, M. J. *et al.* A novel cross-talk in diacylglycerol signaling: the Rac-GAP beta2-chimaerin is negatively regulated by protein kinase Cdelta-mediated phosphorylation. *J Biol Chem* **285**, 16931–16941 (2010).

23. Kasai, H., Ziv, N. E., Okazaki, H., Yagishita, S. & Toyoizumi, T. Spine dynamics in the brain, mental disorders and artificial neural networks. *Nature reviews. Neuroscience* **22**, 407–422 (2021).

24. Cheetham, C. E., Grier, B. D. & Belluscio, L. Bulk regional viral injection in neonatal mice enables structural and functional interrogation of defined neuronal populations throughout targeted brain areas. *Frontiers in neural circuits* **9**, 72 (2015).

25. Goltz, F. Ueber die Verrichtungen des Grosshirns. *Pfluegers Archiv* **42**, 419–467 (1888).

26. Fernandez, L. M. J. & Luthi, A. Sleep Spindles: Mechanisms and Functions. *Physiol Rev* **100**, 805–868 (2020).

27. Snead, O. C., 3rd. Pharmacological models of generalized absence seizures in rodents. *J Neural Transm Suppl* **35**, 7–19 (1992).

28. Goni-Erro, H., Selvan, R., Caggiano, V., Leiras, R. & Kiehn, O. Pedunculopontine Chx10(+) neurons control global motor arrest in mice. *Nat Neurosci* **26**, 1516–1528 (2023).

29. Brown, R. E., Basheer, R., McKenna, J. T., Strecker, R. E. & McCarley, R. W. Control of sleep and wakefulness. *Physiol Rev* **92**, 1087–1187 (2012).

30. Scammell, T. E., Arrigoni, E. & Lipton, J. O. Neural Circuitry of Wakefulness and Sleep. *Neuron* **93**, 747–765 (2017).

31. Chen, X., Leischner, U., Rochefort, N. L., Nelken, I. & Konnerth, A. Functional mapping of single spines in cortical neurons in vivo. *Nature* **475**, 501–505 (2011).

32. Poulet, J. F. & Petersen, C. C. Internal brain state regulates membrane potential synchrony in barrel cortex of behaving mice. *Nature* **454**, 881–885 (2008).

33. Engel, T. A. & Steinmetz, N. A. New perspectives on dimensionality and variability from large-scale cortical dynamics. *Curr Opin Neurobiol* **58**, 181–190 (2019).

34. Lemyre, A., Belzile, F., Landry, M., Bastien, C. H. & Beaudoin, L. P. Pre-sleep cognitive activity in adults: A systematic review. *Sleep Med Rev* **50**, 101253 (2020).

35. Krone, L. B., Yamagata, T., Blanco-Duque, C., Guillaumin, M. C. C., Kahn, M. C. *et al.* A role for the cortex in sleep-wake regulation. *Nat Neurosci* **24**, 1210–1215 (2021).

36. Tossell, K., Yu, X., Giannos, P., Anuncibay Soto, B., Nollet, M. *et al.* Somatostatin neurons in prefrontal cortex initiate sleep-preparatory behavior and sleep via the preoptic and lateral hypothalamus. *Nat Neurosci* **26**, 1805–1819 (2023).

37. Gabbott, P. L., Warner, T. A., Jays, P. R., Salway, P. & Busby, S. J. Prefrontal cortex in the rat: projections to subcortical autonomic, motor, and limbic centers. *J Comp Neurol* **492**, 145–177 (2005).

38. Do, J. P., Xu, M., Lee, S. H., Chang, W. C., Zhang, S. *et al.* Cell type-specific long-range connections of basal forebrain circuit. *eLife* **5** (2016).

39. Baddeley, A. The episodic buffer: a new component of working memory? *Trends in cognitive sciences* **4**, 417–423 (2000).

40. Clark, D. G. & Abbott, L. F. Theory of Coupled Neuronal-Synaptic Dynamics. *Physical Review X* **14** (2024).

41. Lansner, A., Fiebig, F. & Herman, P. Fast Hebbian plasticity and working memory. *Curr Opin Neurobiol* **83**, 102809 (2023).

42. Koch, D., Nandan, A., Ramesan, G. & Koseska, A. Biological computations: Limitations of attractor-based formalisms and the need for transients. *Biochem Biophys*

Res Commun **720**, 150069 (2024).

43. Noguchi, J., Nagaoka, A., Hayama, T., Ucar, H., Yagishita, S. *et al.* Bidirectional in vivo structural dendritic spine plasticity revealed by two-photon glutamate uncaging in the mouse neocortex. *Scientific reports* **9**, 13922 (2019).

44. Yasuda, R., Hayashi, Y. & Hell, J. W. CaMKII: a central molecular organizer of synaptic plasticity, learning and memory. *Nature reviews. Neuroscience* **23**, 666–682 (2022).

45. Volgushev, M., Voronin, L. L., Chistiakova, M. & Singer, W. Relations between long-term synaptic modifications and paired-pulse interactions in the rat neocortex. *Eur J Neurosci* **9**, 1656–1665 (1997).

46. Buonomano, D. V. Distinct functional types of associative long-term potentiation in neocortical and hippocampal pyramidal neurons. *J Neurosci* **19**, 6748–6754 (1999).

47. Weichard, I., Taschenberger, H., Gsell, F., Bornschein, G., Ritzau-Jost, A. *et al.* Fully-primed slowly-recovering vesicles mediate presynaptic LTP at neocortical neurons. *Proc Natl Acad Sci U S A* **120**, e2305460120 (2023).

48. Fu, M., Yu, X., Lu, J. & Zuo, Y. Repetitive motor learning induces coordinated formation of clustered dendritic spines in vivo. *Nature* **483**, 92–95 (2012).

49. Cichon, J. & Gan, W. B. Branch-specific dendritic Ca(2+) spikes cause persistent synaptic plasticity. *Nature* **520**, 180–185 (2015).

50. Feulner, B., Perich, M. G., Chowdhury, R. H., Miller, L. E., Gallego, J. A. *et al.* Small, correlated changes in synaptic connectivity may facilitate rapid motor learning. *Nature communications* **13**, 5163 (2022).

534 # Methods

535

536 ## Animals

537 Dissociated cortical neuron cultures were prepared from embryonic day 17 (E17) ICR
538 mouse embryos (Japan SLC). Sprague–Dawley rats (Sankyo Lab Service) were used to
539 prepare organotypic slice cultures. Neurons from both sexes were mixed in these
540 experiments.

541 For SynC@FPC experiments, 151 male and 162 female C57BL/6J mice (Sankyo
542 Lab Service) received viral injections at postnatal day 1 (P1). Because sex
543 determination at P1 is impractical, both sexes were included, and data from males and
544 females were pooled since no significant sex differences were observed (e.g., Fig. 4b).
545 Thy1-GCaMP6s transgenic mice (C57BL/6N background, Japan SLC) were used for
546 Ca^{2+} imaging experiments in visual cortex (V1). Male C57BL/6J mice aged 4–5 weeks
547 were used for rotarod experiments. In the V1 and M1 experiments, we included only
548 males to ensure consistency with existing normative datasets and to minimize animal
549 numbers, as these paradigms were not specifically designed or statistically powered to
550 detect sex differences.

551 Animals were housed under controlled temperature and humidity conditions and
552 typically maintained on a 12-h light/dark cycle. At the time of experiments, animals
553 were 8–17 weeks old. Food and water were provided ad libitum, except for experiments
554 shown in Fig. 4, Fig. 6, and Extended Data Fig. 8, where the light/dark cycle was
555 reversed to assess behavioural performance during the animals' active (night) period.
556 No formal randomization was performed; however, P1 viral injections were carried out

557 across multiple litters and days without selection for sex, litter, or injection order,
558 effectively randomizing animals across experimental groups. All experimental
559 procedures were approved by the Animal Experimental Committee of the Faculty of
560 Medicine, The University of Tokyo.
561

562 Plasmid constructions and adeno-associated virus (AAV) preparation

563 For dissociated neuronal cultures, the following constructs were generated by PCR and
564 In-Fusion cloning (Takara Bio):
565 pAAV-CaMKII(0.4)-Cre-W; pAAV-hSyn-DIO-mScarlet-W; pAAV-hSyn-DIO-
566 PSDΔ1,2-FRB×3-W; pAAV-hSyn-DIO-FKBP-mVenus-α1-chimerinGAP-W; pAAV-
567 hSyn-DIO-FKBP-mVenus-α1-chimerinGAP-dead(R179G)-W; and pAAV-hSyn-DIO-
568 PSDΔ1,2-FRB-IRES-FKBP-mVenus-α1-chimerinGAP-W.
569 Human FKBP and FRB, and mouse α1-chimerin (Rac1-GAP) cDNAs were cloned from
570 cDNA templates. The GAP-dead mutant was generated by introducing an R179G
571 substitution into α1-chimerin using the following primers (mutated bases underlined):
572 5′-gagagttacggcgtaccagctgctcctg-3′ and 5′-gtacgccgtaactctctggacagg-3′. PSDΔ1,2 was
573 created by deleting amino acids 65–312 from PSD-95. FRB contained the T2098L
574 mutation, as in SynK³, to reduce binding to endogenous FRB and mTOR.
575 For in vivo experiments, the following constructs were packaged into AAV
576 vectors. GAP denotes the RhoGAP domain (amino acids 143–322) of α1-chimerin:
577 pAAV-CaMKII(0.4)-PSDΔ1,2-FRB-IRES-FKBP-HA-GAP-W; pAAV-CaMKII(0.4)-
578 PSDΔ1,2-FRB-IRES-FKBP-HA-GAP-dead(R179G)-W; pAAV-CaMKII(0.3)-
579 PSDΔ1,2-mVenus-FRB×3-W; and pAAV-CaMKII(0.3)-FKBP-mVenus-GAP-W. The
580 AAV-Syn-jGCaMP7f construct was used for calcium imaging.

581 AAVs were produced and titrated as described previously[4]. Briefly, plasmids
582 encoding the AAV vector, pHelper (Stratagene), and pUCmini-iCAP-PHP.eB (Addgene
583 #103005) were transfected into HEK293 (AAV293) cells (Stratagene). After three days,
584 cells were harvested and AAV particles were purified twice by iodixanol gradient
585 centrifugation. Viral genome titres were determined by quantitative PCR. SynC and
586 SynC-dGAP plasmids have been deposited at Addgene (IDs 248572 and 248573).
587

588 **Dissociated culture of neocortex**

589 Cortical neurons were dissociated from embryonic day 17 (E17) ICR mouse embryos
590 and plated at 4.5×10^4 cells cm^{-2} on poly-L-lysine-coated glass-bottom dishes (MatTek,
591 #1.5). Cultures were maintained at 37 °C in 5% CO_2 in Neurobasal medium (Gibco)
592 supplemented with B27 and L-glutamate. At 16 days in vitro (DIV16), cells were
593 transfected with CAG-mScarlet, CaMKII(0.3)-PSDΔ1,2-FRB×3 and CaMKII(0.3)-
594 mVenus-FKBP-GAP at a plasmid ratio of 5:15:1 using Lipofectamine 2000
595 (Invitrogen). After 3–5 days, dual-colour time-lapse images (mVenus and mScarlet)
596 were acquired every 20 min using a confocal microscope (A1R, Nikon). Translocation
597 was induced by adding the A/C heterodimeriser (Takara Bio; 0.5 mM stock in ethanol)
598 at a final concentration of 4 μM, followed by three washes after 10 min. Mean spine
599 density did not differ between WT and GAP-transfected neurons (Extended Data Fig.
600 1g).
601 For analysis of intrinsic spine fluctuations (Extended Data Fig. 1g), the mean
602 change in spine volume (μ) and standard deviation (σ) were computed per 20-min bin
603 during 50–10 min before and 10–130 min after A/C administration[3].

604 To induce chemical LTP, neurons were pre-treated with 50 μM D-APV for 12 h
605 before stimulation, then the medium was replaced with a solution containing (in mM):
606 140 NaCl, 5 KCl, 10 D-glucose, 2 $CaCl_2$, 10 HEPES-Na, 200 μM glycine, and 20 μM
607 bicuculline. After 5–15 min, cultures were returned to the original medium.
608 To induce chemical LTD (Extended Data Fig. 2f), neurons were treated with 20
609 μM NMDA for 5 min in the continuous presence of 400 nM muscimol, which promoted
610 spine shrinkage[5].
611 For histological examination (Extended Data Fig. 1b), cultured cells were washed
612 with phosphate-buffered saline (PBS, pH 7.4) and fixed overnight in 4%
613 paraformaldehyde in PBS, then stored in PBS. Immunohistochemistry was performed as
614 described in the *Histology* section.
615

616 **Hippocampal slice culture**

617 Transverse hippocampal slices (350 μm thick) were prepared from postnatal day 6–8
618 Sprague–Dawley male rats and placed on 0.4-μm culture inserts (EMD Millipore).
619 Slices were maintained at 35 °C in 5% CO_2 in culture medium containing 50% MEM
620 (Invitrogen), 25% HBSS (Invitrogen), 25% horse serum (Invitrogen), and 6.5 g L^{-1}
621 glucose.
622 AAV mixtures were injected into area CA1 on the day of or the day after slice
623 preparation under an upright microscope to confine viral spread within CA1. The
624 injected AAVs were as follows: pAAV-CaMKII(0.4)-Cre (5.0×10^9 gc mL^{-1}); pAAV-
625 hSyn-DIO-PSDΔ1,2-FRB×3 (3.0×10^{13} gc mL^{-1}); pAAV-hSyn-DIO-FKBP-mVenus-
626 GAP (2.0×10^{12} gc mL^{-1}); and pAAV-hSyn-DIO-FKBP-mVenus-dGAP (2.0×10^{12} gc
627 mL^{-1}). After 10–12 days in culture, slices were transferred to a recording chamber and

628 superfused with artificial cerebrospinal fluid (ACSF) containing (in mM): 125 NaCl,
629 2.5 KCl, 2 $CaCl_2$, 0 $MgCl_2$, 1.25 NaH_2PO_4, 26 $NaHCO_3$, 20 glucose, and 200 μM
630 Trolox (Sigma-Aldrich), continuously bubbled with 95% O_2/5% CO_2.
631 Spine enlargement was induced in Mg^{2+}-free ACSF as described previously
632 (Matsuzaki et al., 2004; Ellis-Davies et al., 2007). CDNI-glutamate (1 mM; Nard
633 Institute) was bath-applied for 3–5 min, and photo-uncaging was performed near the
634 target spine. Experiments were conducted at 31 °C.
635 Synaptic transmission was recorded from CA1 pyramidal neurons under whole-
636 cell voltage clamp using patch electrodes (5–7 MΩ) filled with internal solution
637 containing (in mM): 120 potassium gluconate, 20 KCl, 10 disodium phosphocreatine, 4
638 ATP (Mg^{2+} salt), 0.3 GTP (Na^+ salt), and 10 HEPES-KOH (pH 7.3). Evoked synaptic
639 currents were averaged from 10 consecutive stimuli and plotted at each time point
640 (Multiclamp 700B amplifier, Molecular Devices).
641 To isolate receptor-specific components, AP5 (50 μM; Abcam) or NBQX (10
642 μM; MedChemExpress) was applied together with bicuculline (20 μM; Fujifilm) at a
643 holding potential of −70 mV for NMDA- or AMPA-receptor-mediated currents,
644 respectively, whereas GABA-mediated currents were isolated at +30 mV in the
645 presence of AP5 and NBQX. Currents were low-pass filtered at 4 kHz and sampled at
646 10 kHz. Series resistance was ~20 MΩ (uncompensated), and recordings with resistance
647 >30 MΩ were excluded.
648

649 **Mouse AAV and A/C injection**

650 All AAV-mediated transductions were performed using the AAV.PHP.eB capsid.

651 For adult mice (4–5 weeks old; Fig. 2), 1 μL of AAV::CaMKII-SynC (1.0×10^{13} gc
652 mL^{-1}) was pressure-injected unilaterally into V1 (AP −3.0 mm, ML +2.0 mm from
653 bregma) and bilaterally into M1 (AP +1.0 mm, ML ±1.0 mm, DV −1.5 mm from the
654 skull surface) at a depth of 200–450 μm using a syringe pump (RWD) at 0.1 μL min^{-1}.
655 Injections were made through borosilicate glass capillaries without filament (B150-86-
656 10; Sutter Instrument) pulled on a P-1000 micropipette puller (Sutter Instrument).
657 For neonatal mice (postnatal day 1), injection pipettes were fabricated from 10 cm
658 quartz glass capillaries (outer diameter 1.0 mm, inner diameter 0.5 mm; no filament;
659 Q100-50-10, Sutter Instrument) using a P-2000 puller (Sutter Instrument) to yield ~30
660 μm tip diameters. Each pipette was connected via silicone tubing to a 25 μL Hamilton
661 syringe (1702 RN). Viral injections were performed in 250 pups at postnatal day 1 (P1).
662 Each pup was anaesthetized by brief hypothermia on an ice bed and secured in a custom
663 neonatal head holder (Extended Data Fig. 4; Narishige; designed by Mr. Ooishi). The
664 holder arms were positioned vertically at bregma level along the anterior–posterior axis,
665 0.3 mm lateral to the midline on both hemispheres. The glass micropipette was
666 advanced perpendicularly through the skull to a depth of 350–400 μm, and 4 μL of
667 AAV solution was injected using a syringe pump (Neurostar). After recovery on a
668 heating pad, pups were returned to their home cage. The procedure required less than 20
669 min per pup.
670 The A/C heterodimerizer (Takara Bio) was dissolved in N,N-dimethylacetamide
671 (Fujifilm) at 20 mg mL^{-1} and diluted in propylene glycol (Nacalai Tesque) to 2 mg
672 mL^{-1}. Before use, this stock was diluted to 0.4 mg mL^{-1} in diluent (1.2% Polysorbate

673 80, Fujifilm; 27% PEG-300, Fujifilm)[52] and injected intraperitoneally at 1–2 mg kg^{-1}
674 body weight.
675 For Ca^{2+} imaging (Fig. 5; Extended Data Fig. 8), AAV::SynC-fusion (1.2×10^{13} gc
676 mL^{-1}) and AAV::syn-jGCaMP7f (2.0×10^{12} gc mL^{-1}) were co-injected into neonatal
677 pups.
678

679 ## Vital signs

680 EEG, EMG and heartrate (HR) signals were recorded in an electrically shielded open
681 field using a preamplifier (CerePlex Direct, Blackrock) connected to the main amplifier
682 via a lightweight cable. The preamplifier, connected via a 6- or 8-pin adaptor, was
683 secured to the skull using dental cement.
684 At 8–10 weeks of age, mice were implanted with EEG and EMG electrodes under
685 isoflurane anaesthesia. EEG electrodes were placed over the frontal cortex (AP +1.0
686 mm, ML +1.5 mm from bregma), with the ground electrode attached to the skull over
687 the cerebellum. EMG was recorded from two wire electrodes inserted into the m.
688 trapezoideus. To reduce mechanical noise when the mouse bumped into the wall, the
689 EEG/EMG preamplifier was enclosed in a plastic protective frame.
690 EEG signals were filtered at 0.3–250 Hz using a four-pole Butterworth filter and
691 fast-Fourier-transformed to obtain power spectra (0.5-Hz resolution; absolute power in
692 μV^2 $[0.5\ Hz]^{-1}$). Heart rate (HR) was monitored via two subcutaneous wire electrodes,
693 one placed anterior to the heart and the other in the m. pectoralis major, connected to
694 the EEG preamplifier. Data were displayed online and analysed offline using custom
695 Python scripts.

696 Respiration, body temperature and pupil size were monitored in head-fixed mice
697 on a custom turntable (Thorlabs). Running speed was measured using a rotary encoder
698 (Omron). Respiration was detected with a subcutaneous thermocouple electrode placed
699 beneath the nose, and temperature fluctuations were converted to respiratory traces
700 (PTW-401, Unique Medical). Posture and pupil size were video-recorded and quantified
701 using DeepLabCut with custom Python routines.
702

703 **Behaviours**

704 Behavioural experiments were conducted in mice aged 8–17 weeks. Animals were
705 maintained on a 12-h light / 12-h dark cycle, except for the cohorts used in Fig. 4g–i and
706 Fig. 5, in which the cycle was inverted so that the animals' dark phase occurred during
707 the local daytime. Only male mice were used for visual cortical and rotarod experiments
708 to minimize variability due to hormonal cycles.

709 ***Visual cortex imaging***

710 For V1 experiments, male mice were anaesthetized with isoflurane (5% for induction,
711 1.0–1.5% for maintenance), and a midline scalp incision was made. A custom metal
712 head plate was attached to the skull with dental cement (Super-Bond, Sun Medical). A
713 circular craniotomy (4 mm diameter) was made over the left visual cortex (1 mm
714 anterior and 3 mm lateral to the lambda), and the window was sealed with a glass
715 coverslip. Before imaging, chlorprothixene (1.0 mg kg^{-1}; Sigma-Aldrich) was
716 administered intramuscularly, and isoflurane concentration was reduced to 0.2–0.5%.
717 Wide-field calcium imaging was performed using a macro zoom microscope
718 (MVX10, Evident) equipped with a 2× objective (NA 0.25, MVX Plan Apochromat).
719 GCaMP6s fluorescence was excited with a mercury lamp through a GFP mirror unit (U-

720 MGFPHQ/XL; excitation 488 nm, emission 507 nm; Evident). Fluorescence images (4
721 × 4 mm field of view; 512 × 512 pixels) were acquired at 5 Hz using an sCMOS camera
722 (Zyla 4.2, Andor). Drifting grating stimuli (40° diameter) were presented at three
723 horizontal positions on a 32-inch LCD monitor (20 cm from the right eye) using
724 PsychoPy.

725 For each trial, baseline fluorescence (F) was defined as the mean fluorescence
726 during the 1-s period before stimulus onset. The visual response (ΔF) was defined as the
727 mean fluorescence during the stimulus period, and ΔF/F maps were averaged across
728 trials to generate response maps. Imaging data were analysed using custom MATLAB
729 scripts (MathWorks).

730 ***Motor learning***

731 For motor learning (Fig. 2), male mice were trained on a rotarod (MK-610K,
732 Muromachi). Before training, mice were habituated to the stationary rod until calm for
733 ~2 min. During training, the rod accelerated linearly from 0 to 80 rpm over 300 s. Each
734 mouse underwent three 5-min sessions per day. Motor learning consolidation was tested
735 on the following day with one accelerating trial (0–80 rpm).

736 ***State definitions***

737 *State-C* was defined as a period of behavioural arrest with an awake posture (eyes open,
738 head elevated), accompanied by suppressed cortical γ-band (30–80 Hz) power and
739 reduced EMG tone similar to slow-wave sleep (SWS), but without the large δ-band
740 (0.5–4 Hz) power typical of SWS. Only episodes longer than 10 s were counted.
741 *Interm-C* was defined as a transient state showing impaired goal-directed performance
742 after i.p. A/C in SynC@FPC mice, with γ-band power comparable to baseline
743 wakefulness.

744 ***Open-field tasks***

745 Open-field tests were performed either in a large arena (35 × 35 cm) to measure running
746 velocity (Fig. 3) or in a smaller arena (19.4 × 19.4 cm) for close-up videography of laser
747 chasing, food-pellet feeding, and State-C behaviours (Extended Data Movies).

748 For the **laser-dot task**, a green laser pointer (0.5 mW; Sanwa) was projected onto a
749 corner of the small open field for 5 s. A trial was scored as successful (1) if the mouse
750 chased the dot at least once in four presentations, thereby excluding the possibility that
751 the mouse simply failed to attend to the stimulus. WT mice typically chased the laser
752 dot on the floor, whereas SynC@FPC mice neglected it. We eventually used the corner
753 of the field for projection because laser reflections from the floor often produced
754 multiple spurious dots that occasionally complicated interpretation.

755 For the **food-pellet task**, a regular food pellet was dropped into the arena, and the
756 latency from pellet introduction to the first bite while grasping the pellet was measured.
757 Latency periods excluded times when mice were in State-C, which was identified from
758 posture and EEG/EMG. SynC@FPC mice often approached and sniffed the pellet but
759 failed to initiate grasping.

760 In some video recordings, EEG cables were omitted, and State-C was judged
761 solely from behaviour.

762 ***Treadmill***

763 A custom treadmill system was used to monitor locomotion and posture during two-
764 photon Ca^{2+} imaging of M1 activity[51]. The treadmill wheel was mounted on translation
765 stages allowing movement along the caudal–rostral and medial–lateral axes, and the
766 head-fixation height was adjustable. A 45° mirror inside the wheel enabled high-speed
767 videography (Basler acA1920-40um) of simultaneous ventral and lateral views.

768 Wheel rotation was monitored by a rotary encoder (E6B2-CWZ3E, 100 P/R;
769 Omron), and pulses were recorded with CerePlex Direct (Blackrock). The cranial
770 window used a "glass-plug" configuration[52]consisting of two stacked coverslips: a 3-
771 mm-diameter, #1-thickness coverslip placed over a 2-mm-diameter, #3-thickness
772 coverslip (Matsunami Glass) [53].
773 Because behavioural identification was difficult under head fixation, EEG γ-band
774 and EMG signals were used to distinguish State-C from immobile Interm-C. Wheel
775 angular velocity was recorded at 2 kHz and synchronized with imaging via TTL pulses.
776

777 In vivo two-photon imaging

778 For cranial-window surgery for SynC@V1 mice, 8-week-old mice were anaesthetized
779 under isoflurane (5% for induction and 1.0–1.5% for maintenance during surgery) and
780 secured as described above. A circular cranial window was made with stainless-steel
781 trephines (ϕ 2.3 mm; Fine Science Tools) under continuous perfusion of oxygenated
782 ACSF, then covered with a coverslip (ϕ 2.3 mm, No. 0, Matsunami Glass). The
783 coverslip and a custom head plate (DMM 3D printed) were affixed with dental cement
784 (RelyX Unicem2 clicker, 3M). In vivo two-photon calcium imaging was conducted
785 using a two-photon microscope (AXR-MP, Nikon, Japan) equipped with a 20×
786 objective lens (CFI75 Apochromat LWD 20XC W, Nikon) and a femtosecond laser
787 (Insight DS+, Spectra-Physics) at 950 nm was used to excite GCaMP7s. Dendritic
788 spines of GCaMP7s-expressing cells were imaged 60–120 μm below the cortical
789 surface. Series of 500–2000 xy images (8× digital zoom, 512 × 512 pixels) were
790 captured before and after A/C application[54].
791 Two-photon excitation imaging of SynC@FPC mice was performed with a

792 tunable Ti:sapphire laser at an excitation wavelength of 950 nm, using a
793 (XLPLN25XWMP2, 25×/1.05 NA, Olympus) objective, and a resonant scanner set on
794 the treadmill (Fig. 5a). Images were acquired at 30 Hz from forelimb region of M1 (AP
795 + 0 mm, ML +0.5 mm from Bregma). Laser power at the sample did not exceed 50
796 mW, and sessions per mouse were limited to 90 minutes to avoid photodamage.
797 Regions of interest (ROIs) corresponding to neuronal somata (20–180) were extracted
798 with Suite2p (including non-rigid motion correction, ROI detection/classification, and
799 neuropil subtraction). Photobleaching was corrected per ROI by single-exponential
800 fitting to low-activity segments, ΔF/F was computed, and spike trains were inferred
801 with Suite2p's OASIS deconvolution (τ = 400 ms) to obtain firing rates (Fig. 5e).
802

803 **Histology**

804 Three to ten weeks after behavioural experiments, mice were deeply anaesthetized with
805 3% isoflurane and perfused transcardially with PBS (pH 7.4), followed by 4%
806 paraformaldehyde (PFA) in PBS. Brains were post-fixed overnight in 4% PFA at 4 °C
807 and then stored in PBS.
808 For HA-tagged probes, free-floating sagittal sections (50 µm) were cut at 0.5,
809 1.35, 2.35 and 3.55 mm from the midline using a vibratome (VT1200, Leica). Sections
810 were rinsed in PBS, blocked for 1 h at room temperature (RT) in 5% normal goat serum
811 (NGS) in PBST (PBS containing 0.2% Triton X-100), incubated in primary antibody
812 solution (5% normal serum, 0.2% Triton X-100 in PBS) for 24 h at 4 °C, and then in
813 secondary antibody solution under the same conditions for 2 h at RT.
814 ***Primary antibodies:***

815 • Mouse anti-HA (Alexa Fluor 488-conjugated, clone 6E2, #2350S; Cell
816 Signaling Technology), 1:200
817 • Mouse anti-HA (clone 6E2, #2367S; Cell Signaling Technology), 1:200
818 • Rabbit anti-NeuN (EPR12753, ab177487; Abcam), 1:400
819 • Mouse anti-phospho-neurofilament-H (SMI-31, NE1022; Sigma-Aldrich),
820 1:1000
821 • Mouse anti-PSD95 (7E3-1B8, MA1-046; Thermo Fisher), 1:500
822 ***Secondary antibodies:***
823 • Goat anti-rabbit IgG (Alexa Fluor 594, #A-11012; Thermo Fisher)
824 • Goat anti-rabbit IgG (Alexa Fluor 405, #A-31556; Thermo Fisher)
825 • Goat anti-mouse IgG1 (Alexa Fluor 594, #115-587-185; Jackson
826 ImmunoResearch), 1:500
827 Nuclei were counterstained with DAPI (4′,6-diamidino-2-phenylindole; ab228549,
828 Abcam) and mounted using Vectashield Antifade Mounting Medium (Vector
829 Laboratories, Burlingame, CA, USA), then cover-slipped.
830 For mVenus-labelled SynC probes (without HA tag), HA staining was omitted.
831 Sections were rinsed in PBS and directly mounted. Whole-brain serial sections were
832 imaged with an epifluorescence microscope (A1R, Nikon). Z-stack images (4 μm steps;
833 8 μm total for sagittal sections and 17.7 μm for higher magnification views) were
834 aligned and collapsed using NIS-Elements Advanced Research software (Nikon).
835 Imaging and histological analyses were performed blinded using Fiji/ImageJ. SynC
836 expression levels were quantified as Z-scores relative to the s.d. of unlabelled regions
837 and plotted on the Swanson flat map (Extended Data Fig. 4). Cortical thickness at M1

838 was 2.75 ± 0.087 mm (mean ± s.e.m., n = 10) for SynC mice and 2.55 ± 0.097 mm (n =
839 14) for SynC-dGAP mice (Mann–Whitney U = 65, P = 0.05).
840

841 ## Statistical treatments

842 Data are presented as individual observations with mean ± s.e.m. Unless otherwise
843 stated, data were first analysed using non-parametric ANOVA (Kruskal–Wallis),
844 followed by non-parametric multiple comparisons (Steel). When appropriate, Friedman
845 tests or Wilcoxon signed-rank tests (non-parametric *t*-tests versus zero) were applied.
846 Resulting *P* values were corrected for multiple comparisons using the Bonferroni
847 method.

848 For the analysis of pairwise spike correlations, each state or condition within each
849 session was divided into seven non-overlapping windows of 240 frames randomly
850 sampled from the recording. Within each window, ΔF/F traces were temporally binned
851 by three frames. We then computed Spearman's rank correlation (ρ) across cells,
852 extracted upper-triangle coefficients, Fisher-*z* transformed them, averaged across the
853 seven windows, and back-transformed to obtain the pairwise ρ distribution per
854 condition (Fig. 5f). In parallel, cells were partitioned into batches of 20 cells, and for
855 each batch and window we computed: (i) the batch-mean correlation (Fig. 5g; Fisher-*z*
856 mean and back-transformed), (ii) the participation ratio (PR), defined as the square of
857 the total variance (sum of eigenvalues) divided by the sum of squared eigenvalues,
858 indicating the effective dimensionality of neural population activity (Extended Data Fig.
859 8c), and (iii) PCA on the matrix after per-cell *z*-scoring, from which we recorded the
860 number of PCs required to explain 50% of the variance (Extended Data Fig. 8d).

Sample sizes were determined empirically based on previous studies and were comparable to those generally used in the field. No formal randomization was performed; however, because P1 viral injections were conducted across multiple litters and days without selection for sex, litter, or injection order, animals were effectively randomized across experimental groups. Behavioural testing and histological analyses were performed under blinded conditions.

Data and materials availability: All data are available in the main text or the Supplementary Materials. DNA plasmids of SYNCit-C (SynC-fusion) and SYNCit-dGAP (SynC-dGAP-fusion) are deposited to Addgene (ID 248573 and 248572). The code used for the model simulations is available at https://github.com/tkssawada/SynC

Methods References

51. Warren, R. A., Zhang, Q., Hoffman, J. R., Li, E. Y., Hong, Y. K. *et al.* A rapid whisker-based decision underlying skilled locomotion in mice. *eLife* **10** (2021).
52. Goldey, G. J., Roumis, D. K., Glickfeld, L. L., Kerlin, A. M., Reid, R. C. *et al.* Removable cranial windows for long-term imaging in awake mice. *Nat Protoc* **9**, 2515–2538 (2014).
53. Kondo, M., Sehara, K., Harukuni, R., Aoki, R., Sugimoto, S. *et al.* Multimodal dataset linking wide-field calcium imaging to behavior changes in operant lever-pull task in mice. *Sci Data* **12**, 1264 (2025).
54. Hagihara, K. M., Murakami, T., Yoshida, T., Tagawa, Y. & Ohki, K. Neuronal activity is not required for the initial formation and maturation of visual selectivity. *Nat Neurosci* **18**, 1780–1788 (2015).

Acknowledgements

We thank S. Fujii, C. Fujinami, and Y. Hama for technical assistance, Xu, K. Aihara, T. R. Hira, T. Toyoizumi, K. Yoshida, Y. A. Iriki, T. Yamamori, Y. Hayashi, M. Kashiwagi, N. Kitajima, N. Matsumoto and M. Miyano for helpful discussions. During manuscript preparation, the authors used OpenAI's GPT-5 language model for English editing and phrasing refinement under full author supervision. This work was supported by Brain/MINDS 2 (JP24wm0625101 to H.K., S.Z., T.S., S.T., T.H., and T.Y.; JP23wm0625001 to M.M, K.O., S.Y. and JP24wm0625308 to S.Y.; JP24wm0625203 to K.O. and T.H.) from AMED, CREST (JPMJCR21E2 to H.K.; JPMJCR22P1 to K.O.) and FOREST (JPMJFR231T to T.S.) from JST, KAKENHI (JP20H05685 to H.K., S.Z., T.S., and S.Y.; JP23K14385 to T.S.; JP23K14284 to S.T.; JP21H05176 and JP24K02115 to S.Y.; JP21K15612 and JP24K10472 to M.K.; JP22H05160 and JP23H00388 to M.M.; JP25K18580 to T.H.) from JSPS, the Institute for AI and Beyond (to K.O.), and the World Premier International Research Center Initiative (WPI) from MEXT.

Author contributions: The entire experiments were organized by H.K. T.S. led the team (S.Z., H.O., T.A., M.O. and S.K.P.) for synapse-tool design, validation and

behavioural application. H.K. and S.Y. provided guidance. T.H., and K.O. led visual-cortical experiments. S.T., M.K. and M.M. contributed to motor-cortical experiments. The manuscript and figures were prepared jointly by all authors.

Competing Interest: There is no competing interest in this study.

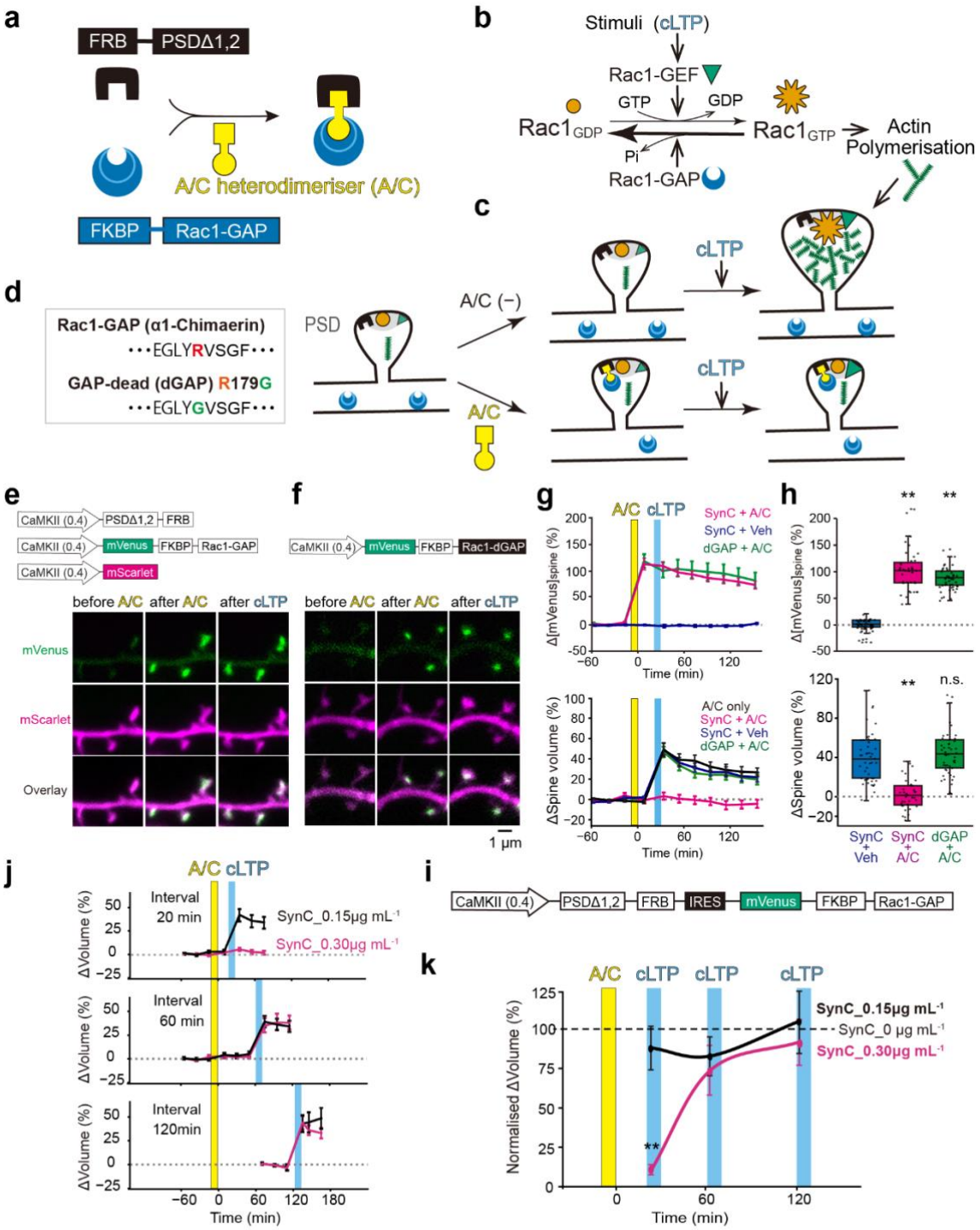
a
FRB
PSDΔ1,2
A/C heterodimeriser (A/C)
FKBP
Rac1-GAP
b
Stimuli (cLTP)
Rac1-GEF
GTP
GDP
Rac1GDP
Rac1GTP
Actin Polymerisation
Pi
Rac1-GAP
c
cLTP
cLTP
d
Rac1-GAP (α1-Chimaerin)
•••EGLYRVSGF•••
GAP-dead (dGAP) R179G
•••EGLYGVSGF•••
PSD
A/C (−)
A/C
e
CaMKII (0.4)
PSDΔ1,2
FRB
mVenus
FKBP
Rac1-GAP
mScarlet
before A/C
after A/C
after cLTP
mVenus
mScarlet
Overlay
f
Rac1-dGAP
1 µm
g
A/C
cLTP
SynC + A/C
SynC + Veh
dGAP + A/C
Δ[mVenus]spine (%)
Time (min)
A/C only
ΔSpine volume (%)
h
n.s.
SynC + Veh
SynC + A/C
dGAP + A/C
i
IRES
j
Interval 20 min
Interval 60 min
Interval 120min
SynC_0.15µg mL-1
SynC_0.30µg mL-1
ΔVolume (%)
Time (min)
k
SynC_0.15µg mL-1
SynC_0 µg mL-1
SynC_0.30µg mL-1
Normalised ΔVolume (%)
Time (min)

Figure 1

911

912 **Fig. 1 | Synaptic chemogenetics, SYNCit-C (SynC).**

913 **a**, Schematic of FRB–FKBP12 dimerisation by the A/C heterodimeriser.
914 **b**, Schematic of G-protein regulation by guanine-nucleotide exchange factors (GEFs) and
915 GTPase-activating proteins (GAPs): Rac1 is activated by a GEF and inactivated through GTP
916 hydrolysis catalysed by a GAP.
917 **c**, FRB is localised to the postsynaptic density (PSD) by fusion with PSDΔ1,2, whereas Rac1-
918 GAP is fused to FKBP and distributed in the cytosol. In the absence of A/C, Rac1 activation by
919 endogenous GEFs induces spine enlargement, whereas A/C application recruits Rac1-GAP to
920 the PSD, inactivating Rac1-GTP and blocking enlargement.
921 **d**, GAP-dead point mutation (R179G) of α1-Chimaerin.
922 **e**, Split-construct design of SynC and representative images showing Rac1-GAP accumulation
923 at spines (green) and inhibition of cLTP-induced spine enlargement (magenta) in dissociated
924 cortical neurons.
925 **f**, SynC-dGAP construct and example images showing Rac1-dGAP translocation to spines and
926 preserved cLTP-induced enlargement.
927 **g**, Quantification of translocation of Rac1-GAP (0.1 μg mL^{-1}) (*e*) or Rac1-dGAP (0.1 μg mL^{-1},
928 top) (*f*) and inhibition of cLTP-induced spine enlargement by SynC + A/C (n = 19 dendrites,
929 151 spines, 6 cells), but not by SynC-dGAP + A/C (n = 26 dendrites, 237 spines, 10 cells) or
930 A/C alone (n = 26 dendrites, 210 spines, 10 cells).
931 **h**, Statistics for (*g*). *Translocation:* Kruskal–Wallis, H = 93.18, $\mathbf{P = 5.85 \times 10^{-21}}$; Steel multiple
932 comparisons (SynC without A/C as control), $\mathbf{P < 0.001}$ for SynC + A/C; $\mathbf{P < 0.001}$ for SynC-
933 dGAP. *Enlargement:* Kruskal–Wallis, H = 58.88, $\mathbf{P = 1.63 \times 10^{-13}}$; Steel multiple comparisons
934 (SynC without A/C as control), $\mathbf{P < 0.001}$ for SynC + A/C; P = 0.599 for SynC-dGAP.
935 **i**, Fusion-construct design of SynC enabling efficient co-expression in vivo.
936 **j**, Transient inhibition of cLTP-induced spine enlargement by the SynC fusion probe following
937 A/C application. Enlargement was completely blocked by SynC (0.3 mg mL^{-1}, red) at 20 min
938 after A/C, but recovered within 1 h. SynC (0.15 mg mL^{-1}, black) produced no significant
939 inhibition, suggesting cooperative Rac1-GAP actions (Extended Data Fig. 1c,e).
940 **k**, Peak amplitudes of spine enlargement at three time points after A/C. n = 17 dendrites (7 cells,
941 3 cultures) for SynC (0.3 mg mL^{-1}) and n = 17 dendrites (8 cells, 3 cultures) for SynC (0.15 mg
942 mL^{-1}). Two-way ANOVA, $F_{2,3}$ = 5.018, **P = 0.0086**; Tukey post hoc, **P = 0.0012** at 20 min after
943 A/C. Amplitudes were normalized to 100% (dashed line) relative to those of SynC (0 mg mL^{-1})
944 at 120 min after A/C (Extended Data Fig. 1c).
945

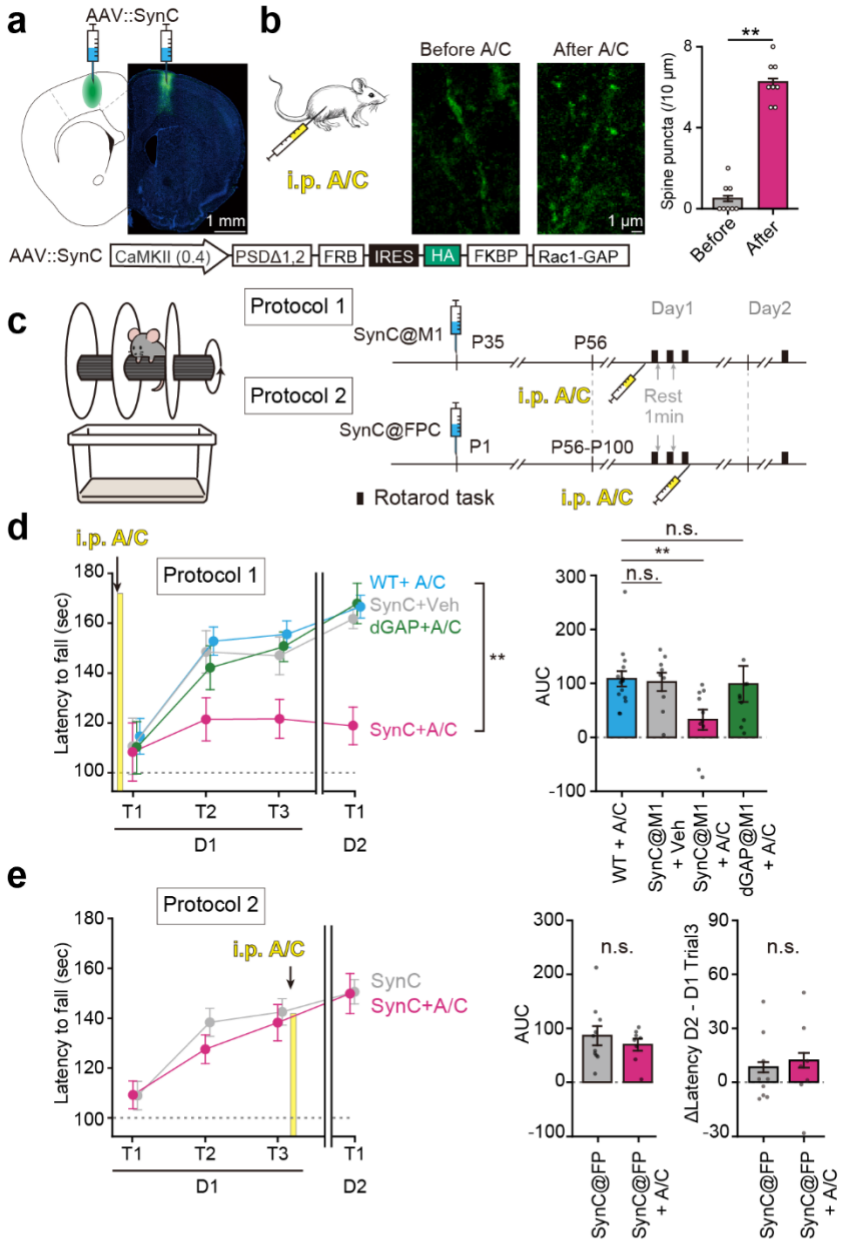
a
AAV::SynC
1 mm
b
i.p. A/C
Before A/C
After A/C
1 µm
Spine puncta (/10 µm)
Before
After
AAV::SynC
CaMKII (0.4)
PSDΔ1,2
FRB
IRES
HA
FKBP
Rac1-GAP
c
Protocol 1
Protocol 2
SynC@M1
P35
P56
Day1
Day2
i.p. A/C
Rest
1min
SynC@FPC
P1
P56-P100
Rotarod task
d
i.p. A/C
Protocol 1
Latency to fall (sec)
WT+ A/C
SynC+Veh
dGAP+A/C
SynC+A/C
T1
T2
T3
D1
D2
AUC
n.s.
WT + A/C
SynC@M1 + Veh
SynC@M1 + A/C
dGAP@M1 + A/C
e
Protocol 2
i.p. A/C
SynC
SynC+A/C
ΔLatency D2 - D1 Trial3
SynC@FP
SynC@FP + A/C

Figure 2

946

Fig. 2 | SynC in the primary motor cortex (M1).

a, Bilateral AAV-SynC injection into mouse M1.

b, Immunohistochemical labelling for the HA tag in M1 of SynC mice before and 30 min after intraperitoneal (i.p.) A/C injection (inset). Magnified dendritic images were used to estimate FKBP–HA–GAP-enriched spines. *n* (dendrites / mice) = 8 / 4 before A/C and 8 / 2 after A/C. Mann–Whitney *U* test, *U* = 6, **P = 0.0015.**

c, Illustration of the rotarod task; the rod was positioned 60 cm above the floor.

d, Rotarod learning curves, quantified as the latency to fall from an accelerated rod (Methods). *n* = 15 wild-type (WT) mice with A/C; 8 SynC@M1 mice with vehicle; 10 SynC@M1 mice after A/C; 11 SynC-dGAP@M1 mice with A/C. Rotarod scores were evaluated by the area under the curve (AUC), calculated for each mouse with the first successful trial set as zero. Statistical analysis was performed using the Kruskal–Wallis test, *H* = 10.54, **P = 0.015**, followed by posthoc Steel's test versus the control group (WT + A/C): P = 0.57 (Z = -0.57) for SynC@M1 + vehicle; **P = 0.0082** (Z = 3.0) for SynC@M1 + A/C; P = 0.298 (Z = 1.44) for SynC-dGAP@M1 + A/C. Only male mice were used for rotarod experiments.

e, Overnight improvement in rotarod performance in SynC@FPC A/C(−) mice (*n* = 10) and SynC@FPC mice given i.p. A/C after training (*n* = 8). Mann–Whitney test comparing SynC@FPC A/C (+) and SynC@FPC A/C (–) groups revealed no significant difference in AUC (P = 0.76, U = 44) or in ΔLatency (D2–D1, trial 3) (*P* = 0.53, *U* = 32.5). Bars represent mean ± s.e.m.

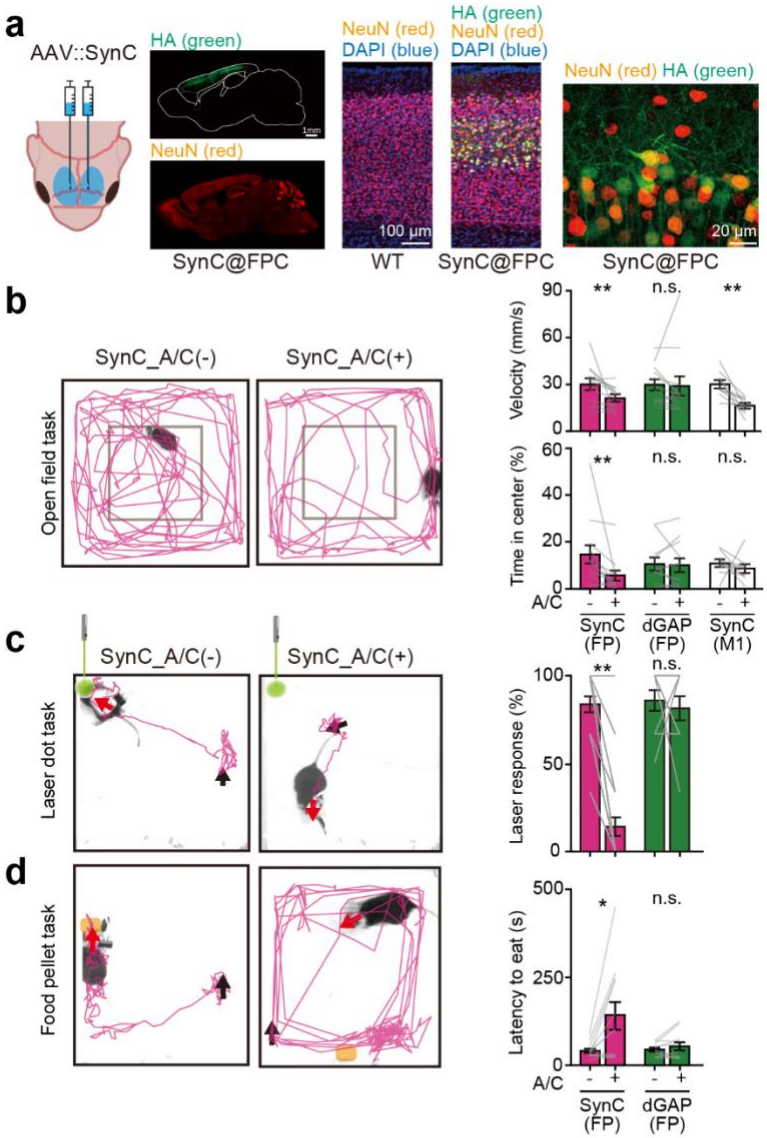
a
AAV::SynC
HA (green)
NeuN (red)
SynC@FPC
NeuN (red)
DAPI (blue)
100 μm
WT
HA (green)
NeuN (red)
DAPI (blue)
SynC@FPC
NeuN (red) HA (green)
20 μm
SynC@FPC
b
SynC_A/C(-)
SynC_A/C(+)
Open field task
Velocity (mm/s)
Time in center (%)
A/C
SynC (FP)
dGAP (FP)
SynC (M1)
c
SynC_A/C(-)
SynC_A/C(+)
Laser dot task
Laser response (%)
d
Food pellet task
Latency to eat (s)
A/C
SynC (FP)
dGAP (FP)

Figure 3

971 **Fig. 3 | SynC in the frontoparietal cortex (FPC).**

972

973 **a**, Neonatal mouse during bilateral cortical AAV-SynC injection together with fast-green dye,
974 and example sagittal sections immunolabelled with anti-HA (top) or anti-NeuN (bottom) 10
975 weeks after FPC SynC injection. Magnified images show layer II/III pyramidal neurons from
976 WT and SynC@FPC mice labelled with DAPI and anti-NeuN to mark neuronal somata, and a
977 further magnified view of cortical cytoarchitecture from a SynC@FPC mouse.
978 **b**, Open-field trajectories of mice before and after i.p. A/C. For average running velocity: $n = 10$
979 SynC@M1 mice before and after i.p. A/C; $n = 12$ SynC@FPC mice; $n = 12$ SynC-dGAP@FPC
980 mice. Bonferroni-corrected Wilcoxon signed-rank test: **P = 0.00195** ($W = 0$) for SynC@M1; **P =**
981 **0.00684** ($W = 6$) for SynC@FPC; $P = 0.151$ ($W = 20$) for SynC-dGAP@FPC. For time spent in
982 the centre: $n = 10$ SynC@M1 mice before and after i.p. A/C; $n = 12$ SynC@FPC mice; $n = 12$
983 SynC-dGAP@FPC mice. Bonferroni-corrected Wilcoxon signed-rank test: $P = 0.0840$ ($W = 10$)
984 for SynC@M1; **P = 0.00684** ($W = 6$) for SynC@FPC; $P = 0.970$ ($W = 38$) for SynC-
985 dGAP@FPC.
986 **c**, Laser-dot-task-induced trajectories in the open field. The arrows indicate the direction from
987 the body centre to the head centre, showing the animal's orientation (black, task start; red, task
988 end). $n = 26$ SynC@FPC mice and $n = 11$ SynC-dGAP@FPC mice before and after i.p. A/C.
989 Bonferroni-corrected Wilcoxon signed-rank test: **P = 8.93 × 10⁻⁶** ($W = 0$) for SynC@FPC; $P =$
990 0.680 ($W = 6$) for SynC-dGAP@FPC.
991 **d**, Food-pellet-task-induced trajectories in the open field. $n = 12$ SynC@FPC mice before and
992 after i.p. A/C, and $n = 11$ SynC-dGAP@FPC mice. Bonferroni-corrected Wilcoxon signed-rank
993 test: **P = 0.0210** ($W = 10$) for SynC@FPC; $P = 0.413$ ($W = 23$) for SynC-dGAP@FPC. Bars
994 represent mean ± s.e.m. Behavioural assays in (b–d) were analysed in animals that exhibited
995 State-C.

996

997

998

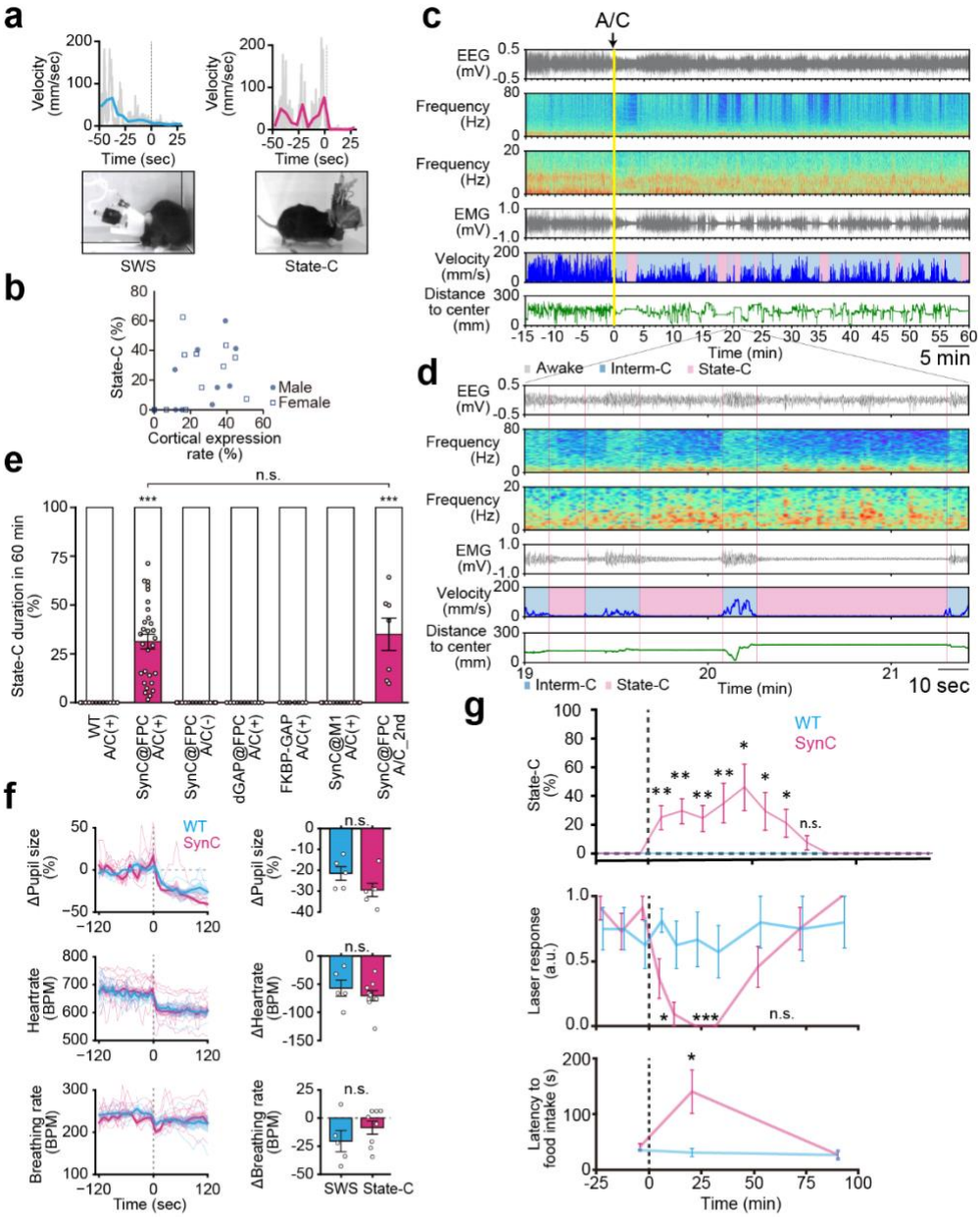
a
Velocity (mm/sec)
Time (sec)
SWS
State-C
b
State-C (%)
Cortical expression rate (%)
Male
Female
c
A/C
EEG (mV)
Frequency (Hz)
EMG (mV)
Velocity (mm/s)
Distance to center (mm)
Time (min)
5 min
Awake
Interm-C
State-C
d
10 sec
e
n.s.
State-C duration in 60 min (%)
WT A/C(+)
SynC@FPC A/C(+)
SynC@FPC A/C(-)
dGAP@FPC A/C(+)
FKBP-GAP A/C(+)
SynC@M1 A/C(+)
SynC@FPC A/C_2nd
f
WT
SynC
ΔPupil size (%)
Heartrate (BPM)
ΔHeartrate (BPM)
Breathing rate (BPM)
ΔBreathing rate (BPM)
SWS
State-C
g
State-C (%)
Laser response (a.u.)
Latency to food intake (s)

Figure 4

Fig. 4 | Non-awake and non-sleep state, State-C in FPC@SynC mice.

a, Examples of locomotor velocity (top) and posture (bottom) at transitions into slow-wave sleep (SWS) in WT mice (left) and into State-C in SynC@FPC mice (right).

b, Correlation between the cortical fraction of SynC-expressing cells and the cumulative duration of State-C within 1 h after A/C administration. All mice without detectable State-C (n = 5) showed minimal labelling, likely due to insufficent viral transduction. There were no differences between male (filled symbols) and female (open symbols) mice.

c,**d**, Representative vital-sign traces from SynC@FPC mice before and after i.p. A/C. From top to bottom: M1 EEG; EEG power spectra (80–0 Hz and 20–0 Hz); EMG; behavioural/EEG-based brain-state classification; and open-field distance from the nearest corner.

e, Percentage of time spent in State-C within 1 h after i.p. A/C. State-C occurred only in SynC@FPC + A/C(+) mice—either at the first or second i.p. A/C injection—but not in A/C(−), SynC-dGAP, FKBP-Rac1-GAP-only, or SynC@M1 mice. State-C was reproducible in the same animals three weeks later.

f, Changes in pupil size (n = 12), heart rate (HR; n = 12 mice), and respiration rate (BR; n = 20 mice) across transitions into State-C on the turntable, relative to transition into SWS of WT (n = 10 mice). Mann–Whitney test: P = 0.70 (U = 70) for pupil size; P = 0.81 (U = 68) for HR; P = 0.85 (U = 74) for BR.

g, Time courses of State-C (top; 9 WT, 8 SynC@FPC mice), laser-dot task (middle; 8 WT, 11 SynC@FPC mice), and food-intake task (bottom; 6 WT, 12 SynC@FPC mice) during 2 h recording at night after i.p. A/C.

For State-C, Bonferroni corrected Mann–Whitney test against 0: **P = 0.0028** (U = 9) at 5–35 min; **P = 0.0086** (U = 13.5) at 45–55 min; P = 0.024 (U = 18) at 65 min; P = 0.144 (U = 27) at 75 min.

Laser-task responses were significantly reduced in SynC@FPC + A/C(+) mice compared with WT (cyan). Friedman test (Ctrl: χ^2 = 3.24, P = 0.36; SynC: χ^2 = 27.8, **P = 4.05 × 10⁻⁶**), followed by Bonferroni-corrected Wilcoxon signed-rank test versus before A/C: after 0–10 min, **P = 0.0047** (W = 0); after 10–30 min, **P = 9.8 × 10⁻⁴** (W = 0); after 50–75 min, P = 0.19 (W = 6.5).

Latency to food intake was increased in SynC@FPC + A/C(+) mice compared with WT (cyan). Friedman test (Ctrl: χ^2 = 0.67, P = 0.72; SynC: χ^2 = 11.48, **P = 3.2 × 10⁻³**), followed by Bonferroni-corrected Wilcoxon test versus before A/C: after 20 min, **P = 0.021** (W = 10); after 90 min, P = 0.103 (W = 11.5).

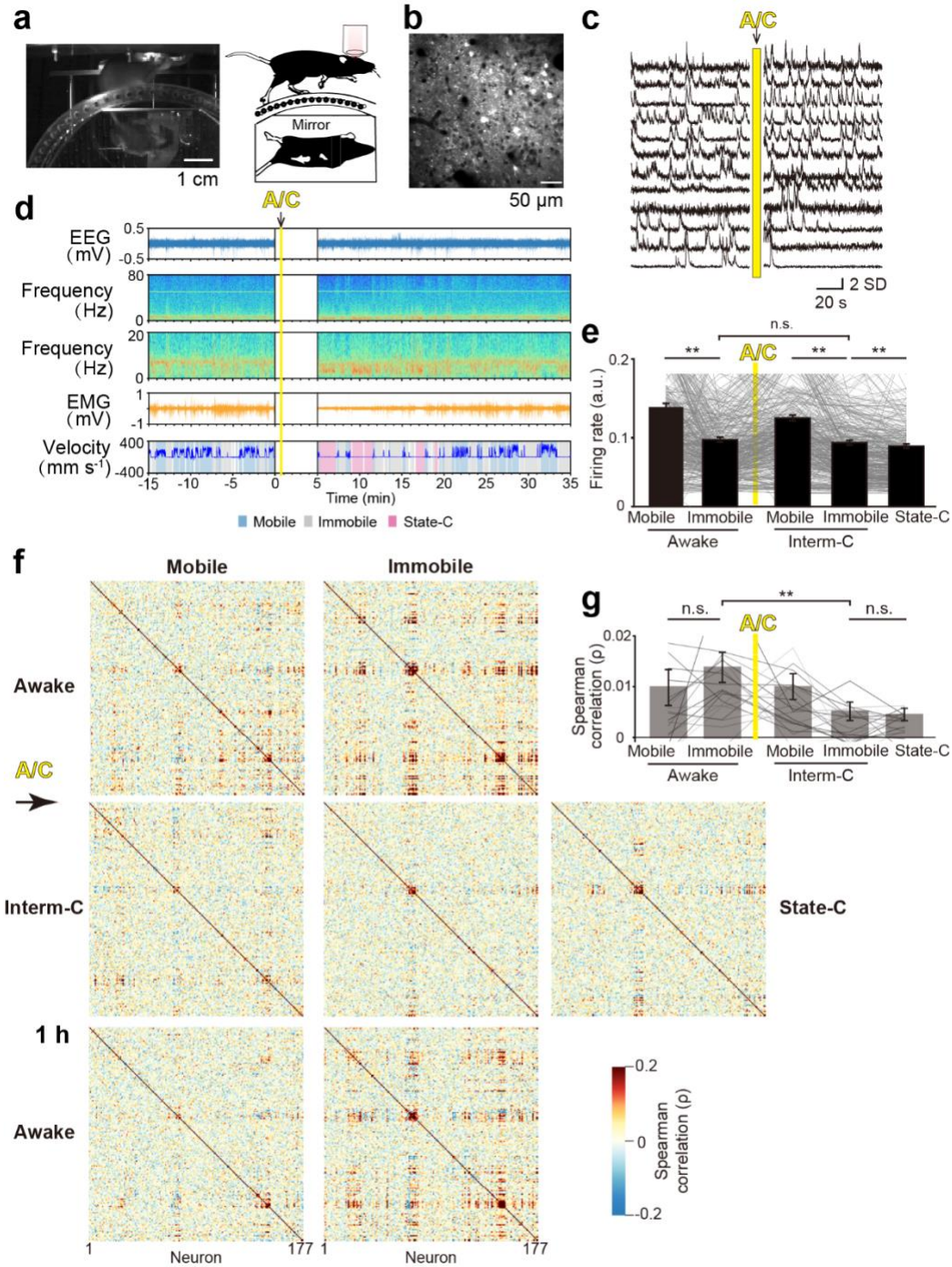

Figure 5

1035

Fig. 5 | Ca^{2+} imaging from M1 in SynC@FPC mice.

a, Illustration of the treadmill setup.

b, Example M1 image from a GCaMP7f-expressing SynC@FPC mouse. Testing was performed during the animals' active (dark) phase.

c, Representative GCaMP7f traces from SynC@FPC mice.

d, Simultaneously recorded EEG, its power spectrum, EMG and running speed with behavioural state classification.

e, Predicted firing rates derived from Ca^{2+} imaging in a SynC@FPC mouse before and after i.p. A/C. Average firing rates are shown for mobile and immobile awake phases before A/C, and for mobile, immobile Interm-C, and State-C phases after A/C (n = 493 cells from 5 SynC@FPC mice). Friedman test, $\chi^2 = 574.6$, $\mathbf{P = 4.9 \times 10^{-123}}$; pairwise Wilcoxon signed-rank test with Bonferroni correction: mobile vs immobile awake, $\mathbf{P = 7.5 \times 10^{-41}}$; mobile vs immobile Interm-C, $\mathbf{P = 9.4 \times 10^{-48}}$; immobile Interm-C vs State-C, $\mathbf{P = 1.1 \times 10^{-9}}$; immobile awake vs immobile Interm-C, $P = 0.071$. Grey lines represent transitions of individual neurons.

f, Pairwise correlations among 177 neurons from one mouse in mobile and immobile states before and after A/C application. Spearman correlation matrices are displayed after hierarchical clustering.

g, Average pairwise Spearman correlation coefficients (n = 21 neuronal assemblies from 5 mice). Friedman test, $\chi^2 = 19.3$, $\mathbf{P = 6.8 \times 10^{-4}}$; pairwise Wilcoxon signed-rank test with Bonferroni correction: mobile vs immobile Awake, $P = 0.16$; mobile vs immobile Interm-C, $\mathbf{P = 2.9 \times 10^{-3}}$; immobile Interm-C vs State-C, $P = 0.56$; immobile Awake vs immobile Interm-C, $\mathbf{P = 2.0 \times 10^{-4}}$.

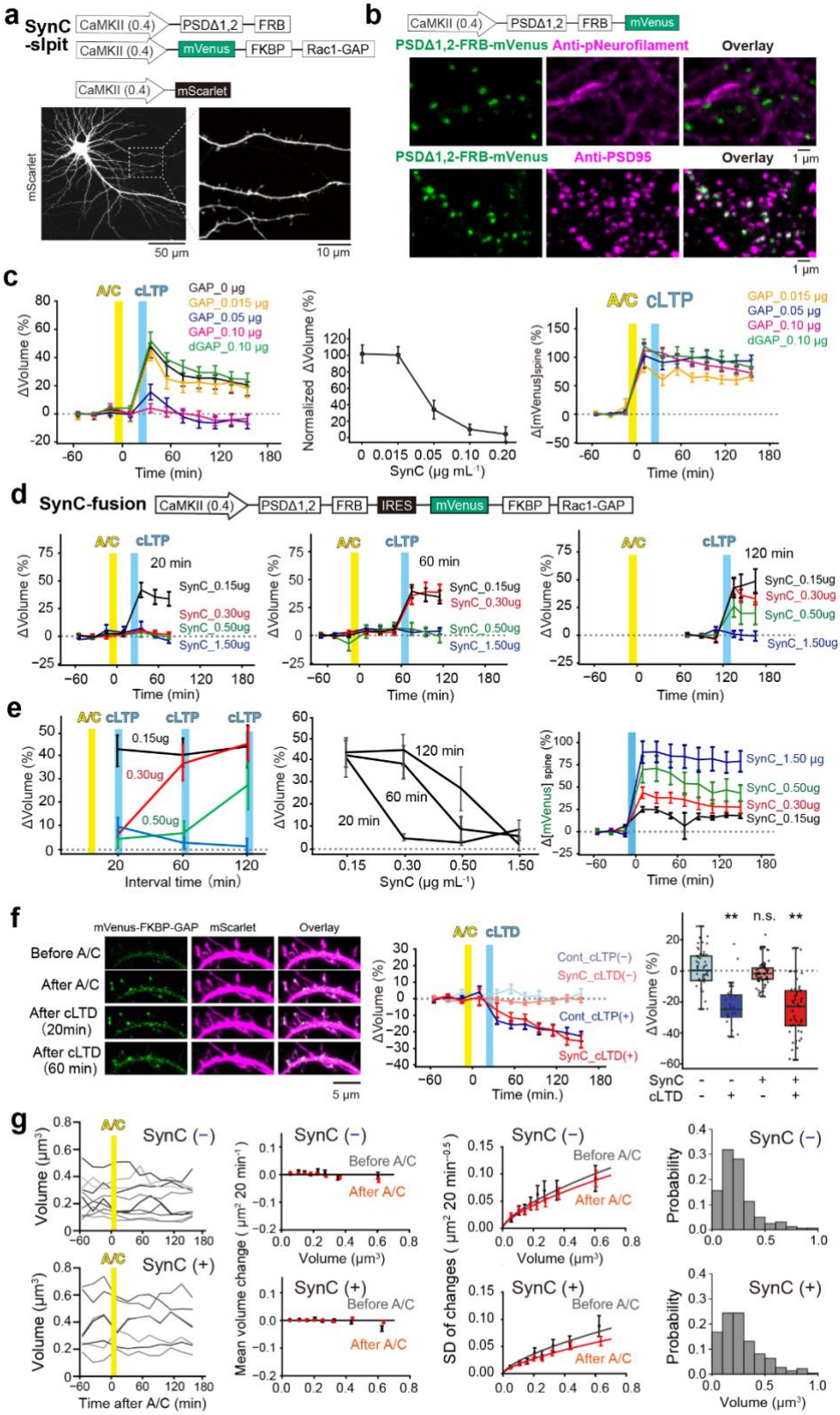

Extended Data Figure 1

1063

1064 **Extended Data Fig. 1 | SynC in neocortical dissociated culture.**
1065 **a,** Example images of dissociated mouse cortical neurons expressing the SynC-split construct
1066 indicated above.
1067 **b,** Simultaneous labelling with PSDΔ1,2–mVenus–FRB and either anti-phospho-neurofilament
1068 (axon, top) or anti-PSD95 (spines, bottom), and their overlays.
1069 **c,** Average blockade of spine enlargement (left), dose dependence of inhibition of spine
1070 enlargement (middle), and translocation of FKBP–mVenus–GAP into spines (right) in cells 20
1071 min after A/C application. Cells were lipofected with 3 mg mL^{-1} PSDΔ1,2–FRB plasmid
1072 (SynC-split). n = 23 dendrites (196 spines, 7 cells) without FKBP–GAP (control); n = 19
1073 dendrites (151 spines, 6 cells) with 0.1 μg mL^{-1} FKBP–GAP; n = 17 dendrites (163 spines, 7
1074 cells) with 0.05 μg mL^{-1}; n = 21 dendrites (164 spines, 21 cells) with 0.015 μg mL^{-1}; n = 26
1075 dendrites (237 spines, 10 cells) with FKBP–dGAP (SynC-dGAP). Dose-dependent inhibition
1076 was tested with Kruskal–Wallis test (H = 67.68, $\mathbf{P = 3.12 \times 10^{-13}}$) followed by Steel multiple
1077 comparisons versus control: $\mathbf{P = 5.00 \times 10^{-6}}$ (H = 23.91) for 0.1 μg mL^{-1} FKBP–GAP; $\mathbf{P = 3.46}$
1078 $\mathbf{\times 10^{-3}}$ (H = 11.60) for 0.05 μg mL^{-1} FKBP–GAP; P = 1.00 (H = 0.0024) for 0.015 μg mL^{-1}
1079 FKBP–GAP; P = 1.00 ($H = 1.00 \times 10^{-4}$) for 0.10 μg mL^{-1} FKBP-dGAP. Relative translocation
1080 of FKBP–GAP quantified by ΔmVenus fluorescence normalised by mScarlet fluorescence of
1081 each spine ($\Delta[\text{mVenus}]_{\text{spine}}$) was uncorrelated with FKBP–GAP concentration, as PSDΔ1,2–
1082 FRB concentration was fixed.
1083 **d,** Average spine enlargement and mVenus translocation at cLTP applied 20 min, 1 h, and 2 h
1084 after A/C treatment in cells lipofected with 1.5, 0.5, 0.3, or 0.15 μg mL^{-1} SynC-fusion plasmid
1085 containing IRES (top).
1086 **e,** Time- and concentration-dependent blockade of spine enlargement and translocation of
1087 SynC–mVenus following transduction with 1.5, 0.5, 0.3, or 0.15 μg mL^{-1} SynC-fusion
1088 plasmids. Relative translocation depended on SynC concentration because PSDΔ1,2–FRB
1089 levels varied accordingly. n = 15 dendrites (6 cells, 3 cultures) for SynC (1.5 mg mL^{-1}); n = 16
1090 dendrites (6 cells, 3 cultures) for SynC (0.5 mg mL^{-1}); n = 17 dendrites (7 cells, 3 cultures) for
1091 SynC (0.3 mg mL^{-1}); and n = 17 dendrites (7 cells, 3 cultures) for SynC (0.15 mg mL^{-1}).
1092 **f,** (Left) Example images of spine shrinkage induced by a cLTD protocol (20 μM NMDA) after
1093 A/C treatment in neurons lipofected with or without SynC-fusion (0.5 μg mL^{-1}). Muscimol (400
1094 nM) was continuously superfused to promote shrinkage. (Center) Time courses of spine-volume
1095 changes induced by the cLTD protocol in the presence of A/C. n = 20 dendrites (206 spines, 6
1096 cells) for non-transfected cells without cLTD; n = 20 dendrites (157 spines, 8 cells) for non-
1097 transfected cells with cLTD; n = 29 dendrites (270 spines, 9 cells) for SynC-fusion-transfected
1098 cells without cLTD; n = 22 dendrites (194 spines, 8 cells) with cLTD. (Right) Kruskal–Wallis
1099 test (H = 43.92, $\mathbf{P = 1.57 \times 10^{-9}}$) followed by post-hoc Steel test: $\mathbf{P = 2.00 \times 10^{-5}}$ (H = 20.41) for
1100 non-transfected cells with cLTD; P = 0.365 (H = 2.42) for transfected cells without cLTD; $\mathbf{P =}$
1101 $\mathbf{2.50 \times 10^{-5}}$ (H = 19.99) for transfected cells with cLTD.
1102 **g,** Spine-volume fluctuations (far left to right center) and stationary volume distributions (far
1103 right) in SynC(−) (top) and SynC(+) (bottom) mice. Initial volume dependence of the mean (left
1104 center) and standard deviation (s.d.; right center) of spine volumes before (black) and after (red)
1105 A/C application in SynC(−) and SynC(+) mice.
1106

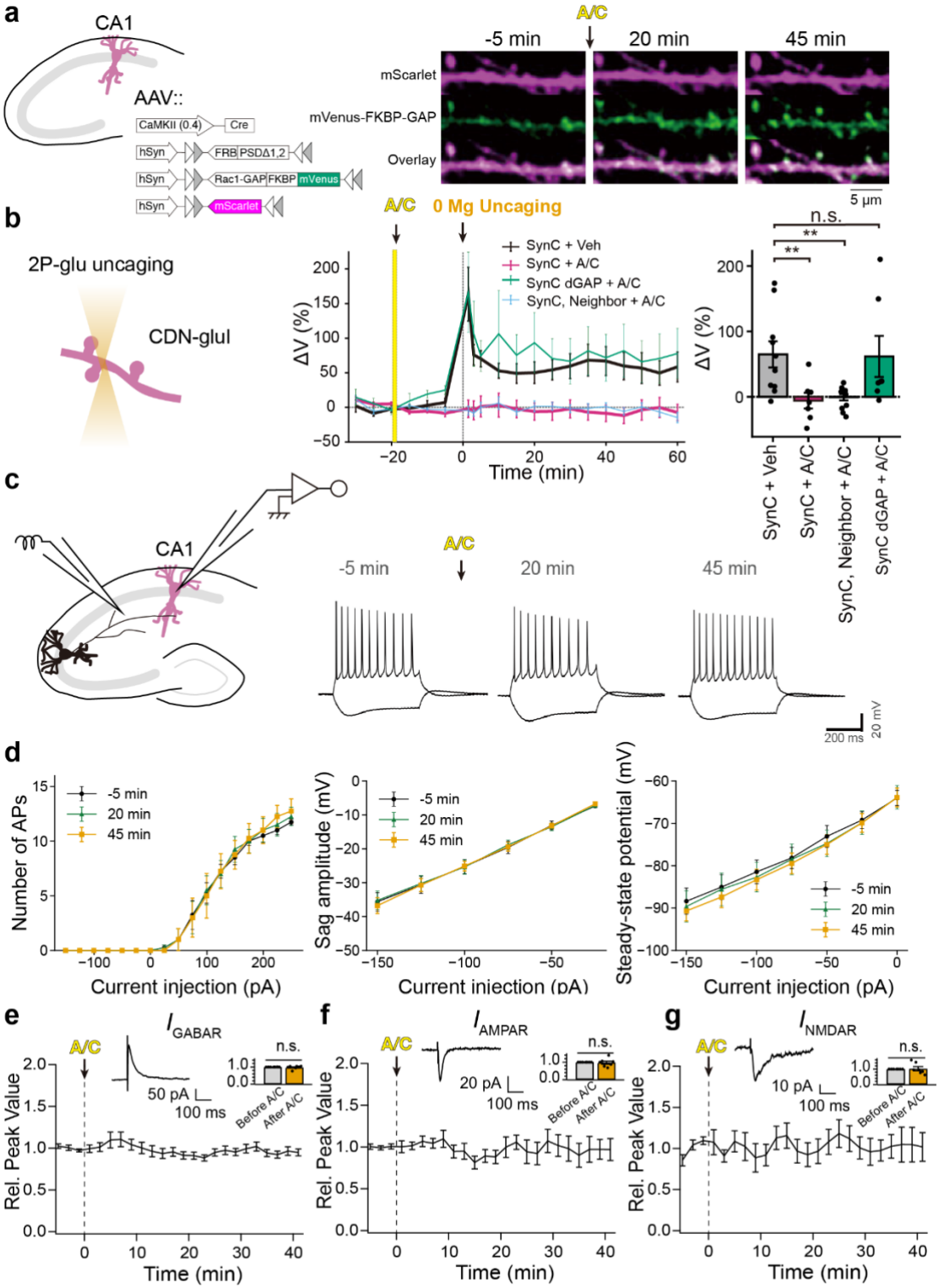

Extended Data Figure 2

1107

Extended Data Fig. 2 | SynC in hippocampal slice culture.

a, Schematic of the experiment in rat hippocampal slice culture and representative dendritic images. CA1 pyramidal neurons were transfected with AAVs encoding SynC constructs for 2 weeks (Methods). Filler (mScarlet, left), mVenus-FKBP-GAP (middle) and merged images (right) are shown before and after A/C application.

b, Two-photon glutamate uncaging in CA1 pyramidal neurons expressing SynC or SynC-dGAP. A/C was added 20 min before uncaging and did not affect spine volume. Comparison of spine enlargement among four conditions: SynC A/C(−), SynC A/C(+), neighbours, and SynC-dGAP A/C(+). n = 10 spines (3 slices, 2 rats), 7 spines (2 slices, 2 rats), 12 neighbouring spines (2 slices, 2 rats) and 7 spines (2 slices, 2 rats), respectively. Kruskal–Wallis test, H = 14.91, $\mathbf{P = 1.89 \times 10^{-3}}$; followed by Steel's multiple comparisons (SynC A/C(−) as control): SynC A/C(+), $\mathbf{P = 9.26 \times 10^{-3}}$; neighbours, $\mathbf{P = 8.09 \times 10^{-3}}$; SynC-dGAP A/C(+), P = 0.813. Bars represent mean ± s.e.m.

c, Schematic of slice-recording setup for current-evoked action potentials and electrical stimulation-evoked synaptic currents.

d, Summary graphs show AP firing frequency as a function of injected current (left), sag amplitude (middle), and steady-state potential (right) in neurons expressing SynC constructs (n = 4). Sag amplitude was defined as the difference between the voltage minimum and the steady-state value. To measure the steady-state potential 20 min and 45 min after A/C administration (panel c), a bias current was injected to maintain the initial resting potential. Two-sided repeated-measures ANOVA for number of APs ($F_{(2,6)}$ = 0.096, P = 0.91), sag amplitude ($F_{(2,6)}$ = 1.22, P = 0.36), and steady-state potential ($F_{(2,6)}$ = 1.34, P = 0.33). No significant differences were observed across time points.

e–**g**, Voltage-clamp recordings of inhibitory (e, GABA_A) and excitatory (f, AMPAR; g, NMDAR) currents in the presence of selective blockers. GABA_A currents were evoked at +30 mV in NBQX (10 μM) and APV (50 μM). AMPAR currents were evoked at −70 mV in APV (50 μM) and bicuculline (20 μM), and abolished by NBQX (10 μM). NMDAR currents were evoked at −70 mV in NBQX (10 μM) and bicuculline (20 μM). A/C had no effect in any case (n = 7 cells each; Wilcoxon signed-rank test: GABA_A, W = 12, P = 0.81; AMPAR, W = 12, P = 0.81; NMDAR, W = 13, P = 0.94).

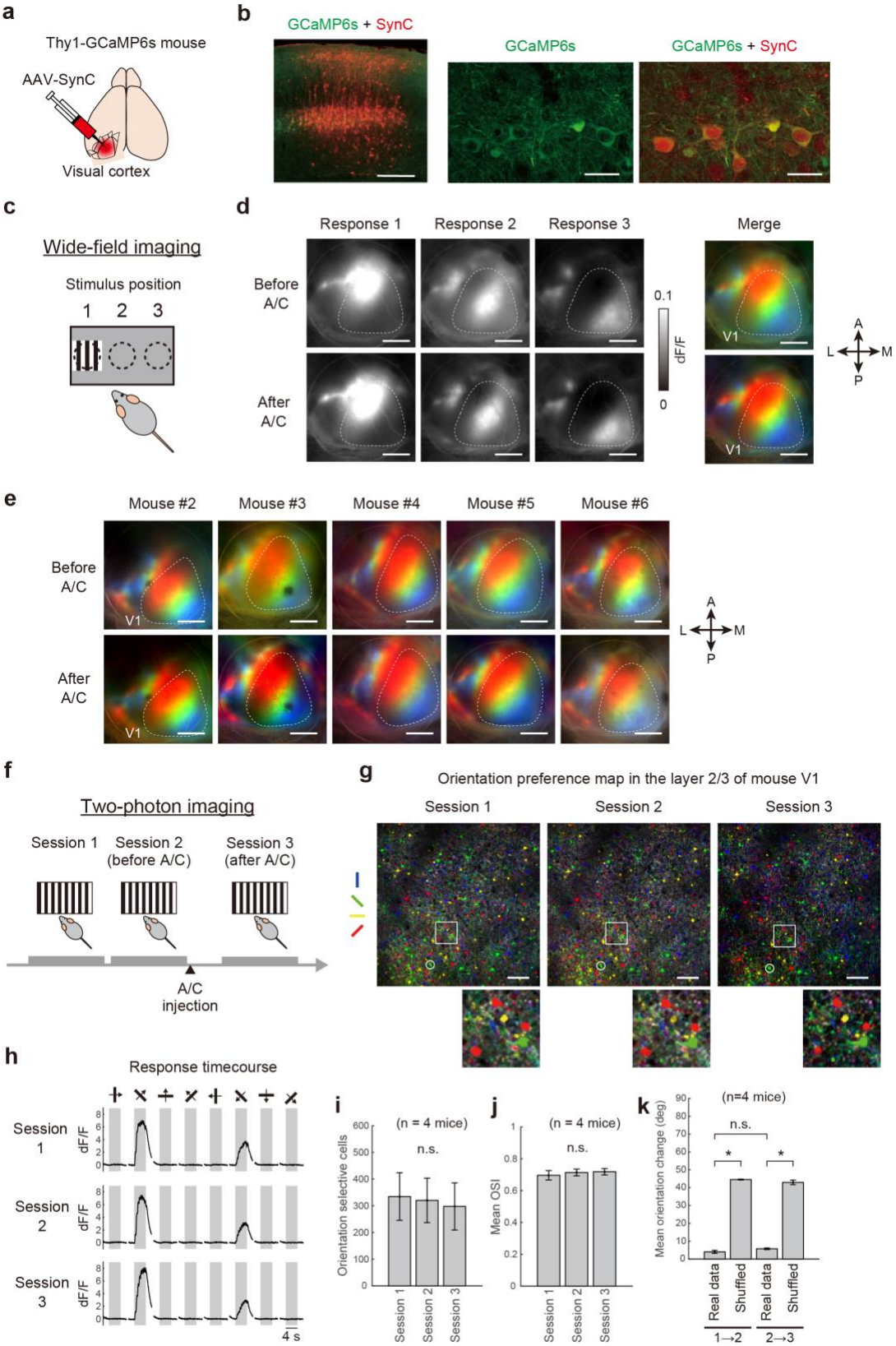

Extended Data Figure 3

1138

Extended Data Fig. 3 | SynC expression and functional assessment in the mouse primary visual cortex (V1).

a, Injection of AAV::SynC (Fig. 2a) into V1 of Thy1-GCaMP6s mice.

b, Histochemical examination of GCaMP6s and SynC expression in the visual cortex.

c, Retinotopic mapping of the visual cortex using wide-field calcium imaging. Grating stimuli (40° diameter) were presented at three horizontal positions on the monitor, separated by 40°.

d, Visual response maps to the three grating stimuli (left). Merged maps visualizing retinotopic organization before (top) and after i.p. A/C (bottom).

e, Retinotopic organization was unchanged after A/C injection across six mice (one in d included).

f, Two-photon calcium imaging in V1. To evaluate the effects of SynC on V1 neuronal response properties, three imaging sessions (sessions 1–3) were performed. Each session consisted of 20 trials of drifting-grating presentation. Baseline tuning stability was assessed between sessions 1 and 2, and A/C effects were tested between sessions 2 and 3.

g, Orientation-preference maps obtained in sessions 1–3 (top). Insets show higher-magnification views of the regions indicated by white squares (bottom).

h, Trial-averaged calcium traces of a representative neuron shown in g (white circle). Gray shading indicates the period of visual stimulus presentation.

i, Number of orientation-selective neurons across sessions (n = 4 mice; one-way ANOVA, P = 0.96).

j, Mean orientation selectivity index (OSI) across sessions (n = 4 mice; one-way ANOVA, P = 0.79).

k, Average changes in the preferred orientation of orientation-selective neurons across sessions (n = 4 mice; paired t-test with Bonferroni correction): sessions 1–2, $\mathbf{P = 9.19 \times 10^{-5}}$ (real vs. shuffled data); sessions 2–3, $\mathbf{P = 2.39 \times 10^{-4}}$ (real vs. shuffled data); sessions 1–2 vs. 2–3 (real data), P = 0.569.

Scale bars: 50 μm (b, right); 100 μm (b, left; g); 1 mm (d, e). Error bars represent mean ± s.e.m.

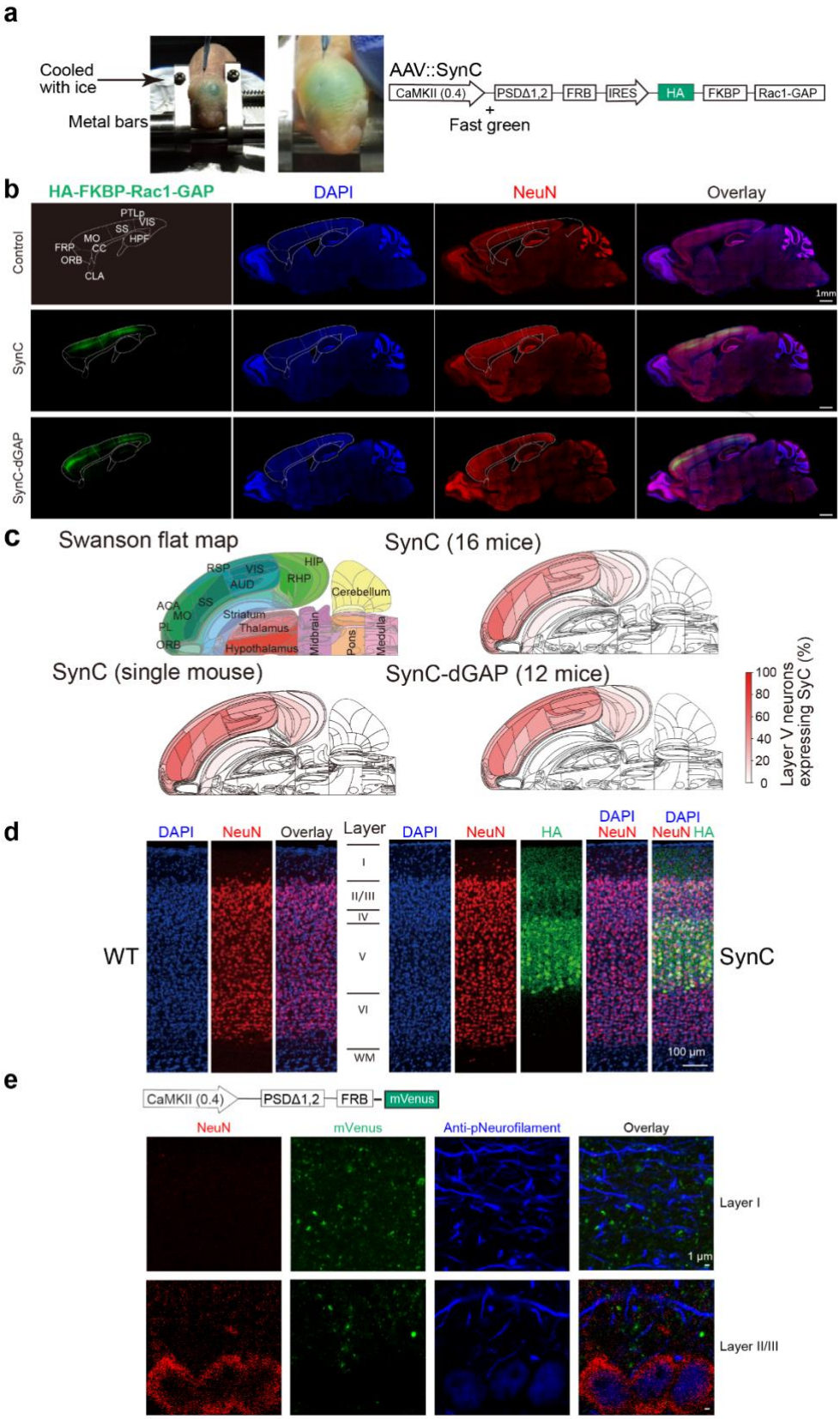

Extended Data Figure 4

1169

1170 **Extended Data Fig. 4 | Anatomy of SynC@FPC mice.**
1171 **a**, Schematic illustration of neonatal pup injection and the AAV vector design.
1172 **b**, Representative sagittal (1.35 mm ML) sections from non-injected control, SynC@FPC, and
1173 SynC-dGAP@FPC mice stained with anti-HA-tag, anti-NeuN, and DAPI. HA-FKBP-GAP was
1174 not efficiently transported to axons; subcortical regions containing long neocortical axons were
1175 largely immunonegative.
1176 **c**, Swanson flat map showing SynC expression levels quantified by HA immunoreactivity in
1177 layer V pyramidal neurons. The percentage of labeled cells is pseudocolor-coded.
1178 **d**, Enlarged overlays of M1 laminar structures in WT and SynC@FPC mice.
1179 **e**, Distribution of PSDΔ1,2-FRB-mVenus in the cortex co-labeled with anti-NeuN and anti-
1180 phospho-neurofilament (axons and perinuclear structures). No overlap was observed between
1181 axonal and mVenus signals. mVenus-labeled spines were located adjacent to axons in layer I.
1182 Exclusion of mVenus signal from somata (NeuN-positive) and dendritic shafts in layers II/III
1183 were confirmed.
1184
1185
1186
1187

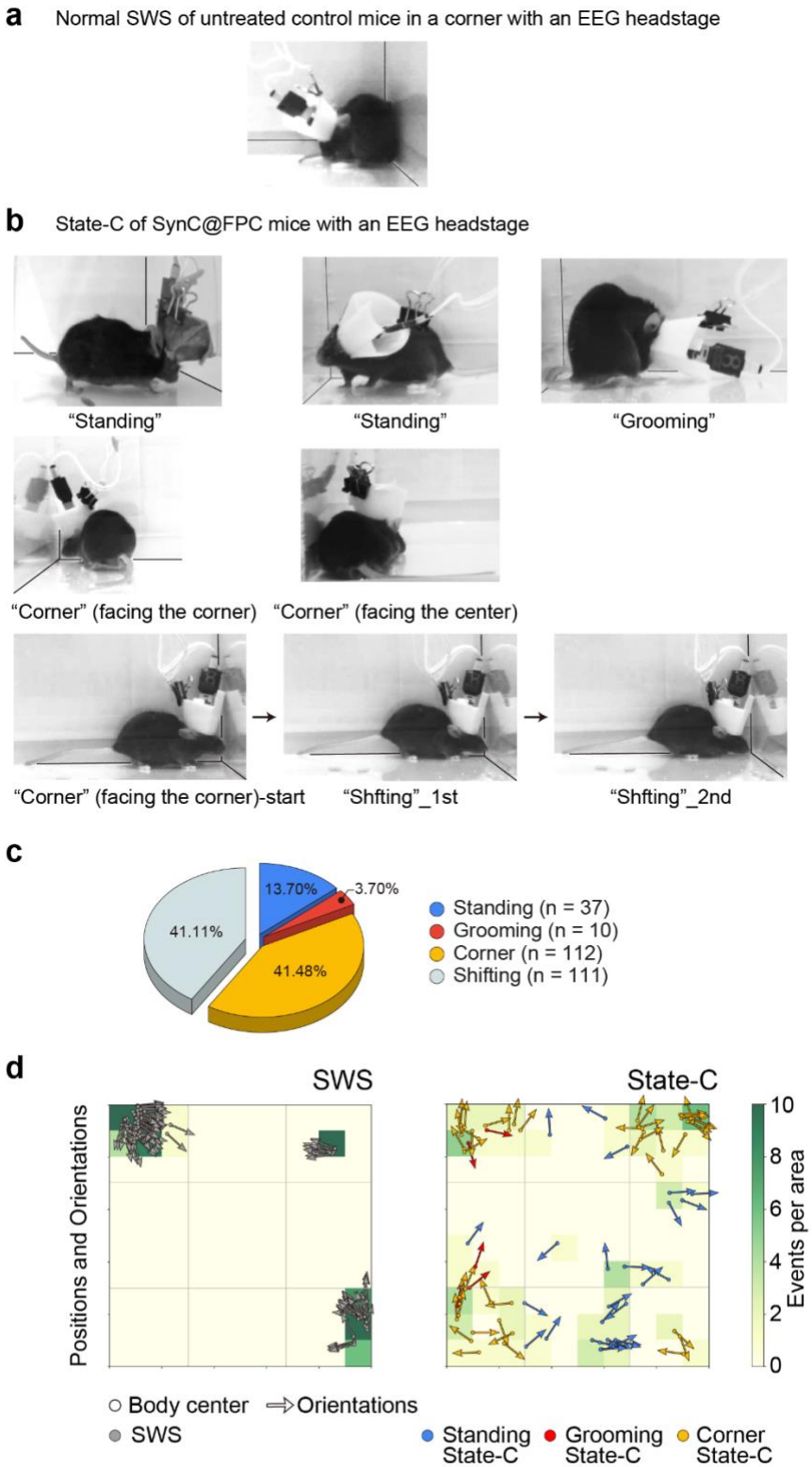

Extended Data Figure 5

Extended Data Fig. 5 | State-C postures and positions.

a, Image of a WT mouse in SWS, positioned at a corner of the open field and facing toward the center.

b, Images of SynC@FPC mice in State-C showing “standing,” “grooming,” and “corner” postures, which occurred during running, grooming, and corner navigation, respectively. Mice typically faced either a corner or the center of the open field (19.4 × 19.4 cm). The “shifting” posture most frequently occurred in the “corner” condition and gradually transitioned to a more sitting posture during short Interm-C episodes confirmed by enhanced EEG γ-band power.

c, Composition of the four State-C postures.

d, Positions and orientations of the mice during SWS (left, n = 6, 112 epochs in total) and State-C (right, n = 5, 80 epochs in total) in the open field (19.4 × 19.4 cm). Dwell times at each region are pseudocolor-coded. SWS occurred consistently in corners facing the centre, whereas State-C occurred at various positions and orientations across the field.

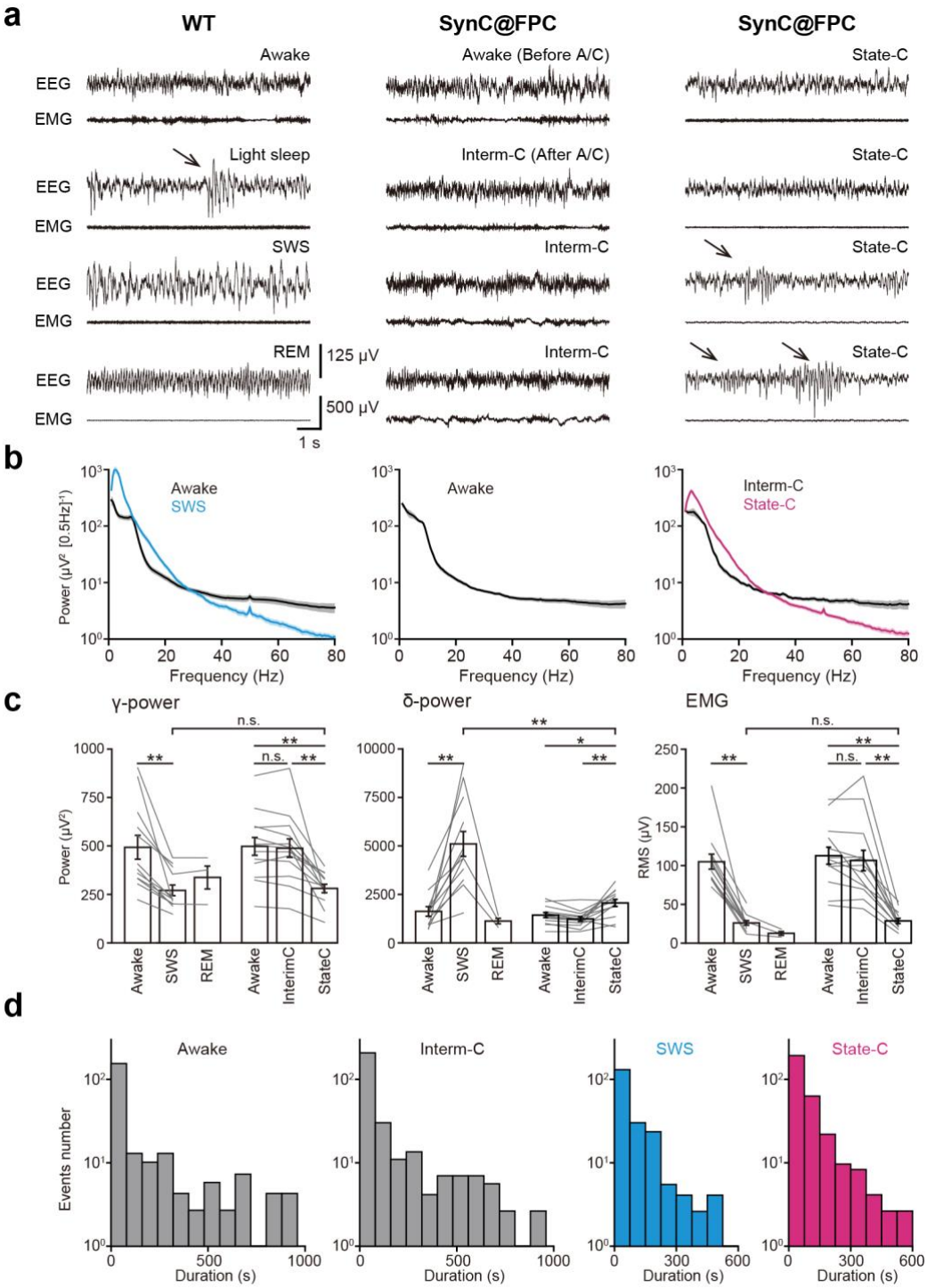

Extended Data Figure 6

1204

Extended Data Fig. 6 | EEG states of SynC@FPC mice.

a, Representative EEG and EMG traces during awake, light sleep, SWS, and REM sleep in wild-type mice (left); during awake before and Interm-C after i.p. A/C injection in SynC@FPC mice (middle); and during State-C after A/C (right). Arrows indicate sleep spindles.

b, EEG power spectra for SWS and awake in control animals (left); awake state in SynC@FPC mice before A/C (middle); and State-C and Interm-C after A/C (right).

c, Quantification of EEG and EMG across distinct states.

(Left) γ-power (30–80 Hz) in awake, SWS and REM (n = 12 WT mice) and in awake, Interm-C and State-C (n = 13 SynC@FPC mice). Wilcoxon signed-ranks test (WT, awake versus SWS): W = 0, $\mathbf{P = 4.9 \times 10^{-4}}$. For SynC@FPC, Friedman test ($\chi^2 = 19.8$, $\mathbf{P = 4.9 \times 10^{-5}}$) followed by pairwise Wilcoxon signed-rank tests with Bonferroni correction: P = 0.24 for awake versus Interm-C; $\mathbf{P = 2.4 \times 10^{-4}}$ (W = 0) for awake versus State-C; $\mathbf{P = 2.4 \times 10^{-4}}$ (W = 0) for Interm-C versus State-C. Mann-Whitney U test for SWS versus State-C: P = 0.53 (U = 66).

(Middle) δ-power (0.5–4 Hz) in awake, SWS and REM, and in awake, Interm-C and State-C. Wilcoxon signed-rank tests (WT, awake versus SWS): W = 0, $\mathbf{P = 4.9 \times 10^{-4}}$. For SynC@FPC Friedman test ($\chi^2 = 15.4$, $\mathbf{P = 4.6 \times 10^{-5}}$) followed by pairwise Wilcoxon signed-rank tests with Bonferroni correction: $\mathbf{P = 1.2 \times 10^{-3}}$ (W = 3) for Awake versus Interm-C; $\mathbf{P = 4.6 \times 10^{-3}}$ (W = 7) for awake versus State-C; $\mathbf{P = 1.7 \times 10^{-3}}$ (W = 4) for Interm-C versus State-C. Mann-Whitney U test for SWS versus State-C: $\mathbf{P = 1.7 \times 10^{-4}}$ (U = 145).

(Right) EEG RMS amplitudes δ-power (0.5–4 Hz) in awake, SWS and REM, and in awake, Interm-C and State-C. F Wilcoxon signed-rank tests (WT, awake versus SWS): $\mathbf{P = 4.9 \times 10^{-4}}$ (W = 0). For SynC@FPC mice, Friedman test ($\chi^2 = 19.8$, $\mathbf{P = 4.9 \times 10^{-5}}$) followed by pairwise Wilcoxon signed-rank tests with Bonferroni correction: P = 0.27 (W = 29) for Awake vs Interm-C; $\mathbf{P = 2.4 \times 10^{-4}}$ (W = 0) for Interm-C vs State-C; $\mathbf{P = 2.4 \times 10^{-4}}$ (W = 0) for Awake vs State-C; Mann-Whitney U test for SWS versus State-C: P = 1.0 (U = 78).

d, Distributions of awake (n = 12 mice) and Interm-C durations (n = 13 mice), and of SWS (n = 12 mice) and State-C durations (n = 13 mice).

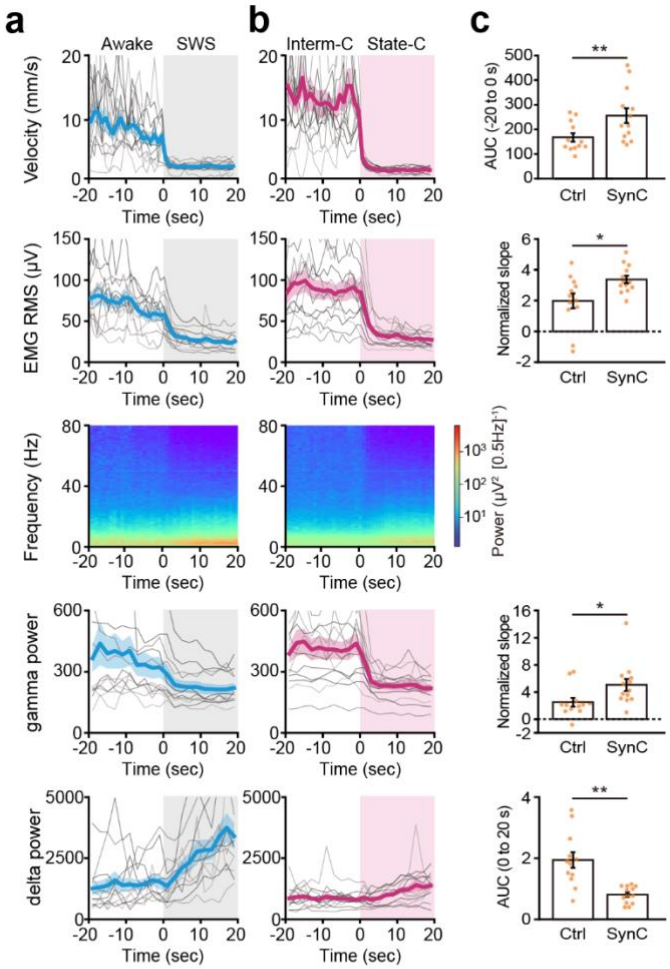

Extended Data Figure 7

Extended Data Fig. 7 | State transitions from State-C to Interm-C.

a,b, From top to bottom: locomotor velocity, root mean square (RMS) of EMG, EEG spectrogram, and γ- and δ-band power during transitions from Awake to SWS (n = 12 mice, **a**) and from Interm-C to State-C within 2 h after i.p. A/C administration (n = 13 mice, **b**). Traces are aligned to the transition onset (t = 0). Each per-mouse trace represents the mean of 3–16 transition events for that mouse; bold lines indicate across-mouse means.

c, Quantitative comparisons of Awake→SWS and Interm-C→State-C transitions. For each mouse, areas under the curve (AUC) were compared using two-sided Mann–Whitney U tests: **P = 4.5 × 10^{-4}** (U = 32) for locomotor velocity; P = 0.013 (U = 143) for δ-band power. Slope ratios were calculated as the slope over −3 to +1 s normalized by the slope over −10 to +10 s and compared using two-sided Mann–Whitney U tests: **P = 0.021** (U = 35) for RMS of EMG; **P = 0.013** (U = 32) for γ-band power.

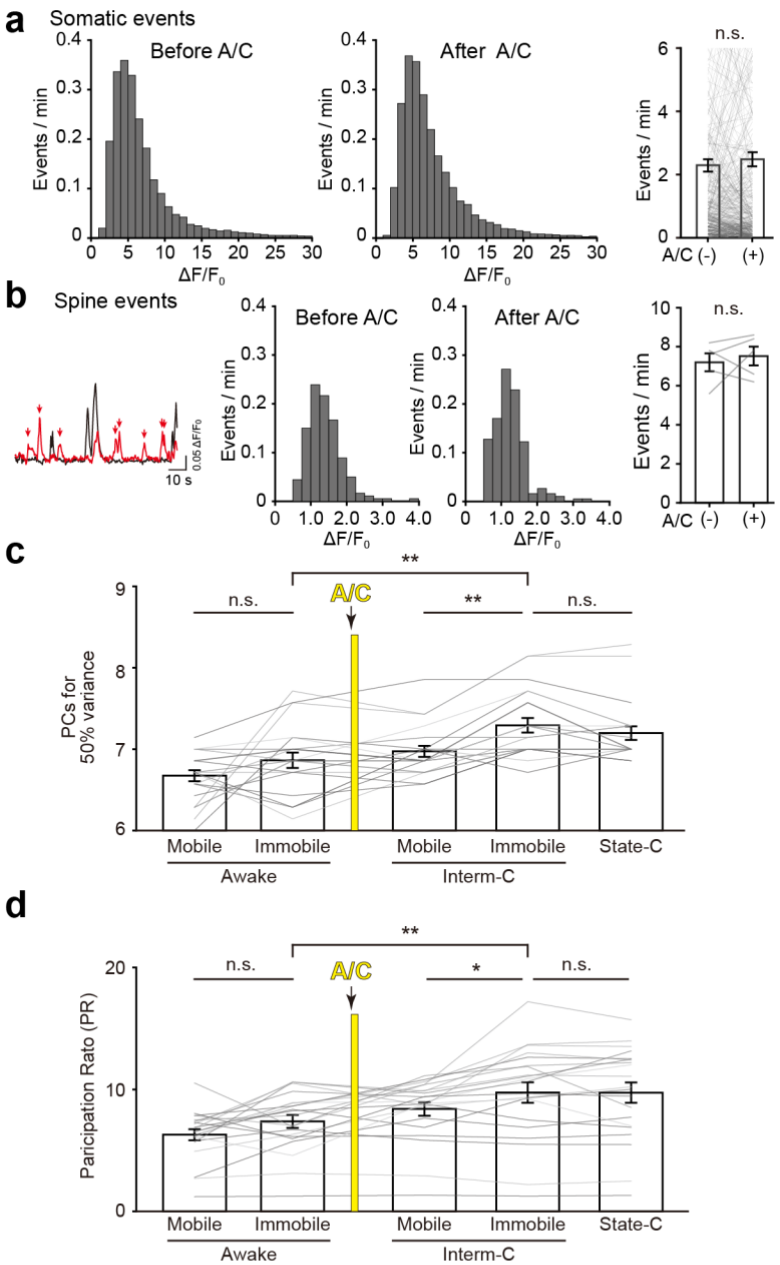

Extended Data Figure 8

1253

Extended Data Fig. 8 | Analysis of Ca^{2+} imaging data.

a, Distributions of detected GCaMP7f event amplitudes ($\Delta F/F_0$) per minute before (left) and after (center) A/C heterodimerizer administration, and event frequency (right). n = 493 cells (5 mice). Mean amplitudes were equivalent. Wilcoxon signed-rank test: P = 0.29 ($W = 4.8 \times 10^4$).

b, Spine Ca^{2+} transients (red) isolated from adjacent dendritic shafts (black). The amplitude distributions and mean amplitudes were unaffected by i.p. A/C administration. Mann-Whitney U test: P = 0.60 (U = 9.5).

c, Number of principal components (PCs) accounting for 50% of the total variance across cells (n = 21 cell assemblies from 5 mice). Friedman test ($\chi^2 = 49.4$, $\mathbf{P = 4.8 \times 10^{-10}}$) followed by pairwise Wilcoxon signed-rank tests with Bonferroni correction: mobile vs immobile awake, P = 0.23; mobile vs immobile Interm-C, $\mathbf{P = 5.7 \times 10^{-4}}$; immobile Interm-C vs State-C, P = 0.077; immobile awake vs immobile Interm-C, $\mathbf{P = 8.6 \times 10^{-5}}$.

d, Participation ratio (PR) for mobile and immobile awake phases before A/C, and for mobile, immobile Interm-C, and State-C after i.p. A/C administration (n = 21 cell assemblies from 5 SynC@FPC mice). Friedman test ($\chi^2 = 29.2$, $\mathbf{P = 7.1 \times 10^{-6}}$) followed by pairwise Wilcoxon signed-rank tests with Bonferroni correction: mobile vs immobile awake, P = 0.029; mobile vs immobile Interm-C, P = $\mathbf{3.3 \times 10^{-3}}$; immobile Interm-C vs State-C, P = 0.61; immobile awake vs immobile Interm-C, $\mathbf{P = 5.1 \times 10^{-4}}$.

Extended Data Table 1 |
Orientation map distinguishing Interm-C and State-C from canonical states

Mouse-focused summary table comparing wakefulness-related, sleep, and arrest-like states.

State (ordered)	EEG signature	EMG	Behaviour	Autonomic / Key features
Awake (reference)	Low-amp fast; γ✓; δ low	High	Exploration; goal-directed	Pupil dilated; HR high-norm; resp ≈; textbook wake
Interm-C (this study)	**Low-amp fast; γ✓; δ low**	**High**	**Locomotor-active; goal-directed control ↓**	**Pupil/HR ≈; resp ≈; decorrelation↑**
State-C (this study)	**γ↓; small δ↑; isolated spindles sometimes✓; no SWD**	**Low**	**Behavioural arrest with exponential durations、similar to SWS**	**Isolated spindle; Miosis; mild HR↓; resp ≈**
SWS (deep NREM)	δ↑↑; high-amp; spindles ±	Low	Sleep posture;	Miosis; HR↓; resp slow; high arousal threshold
REM sleep	θ-dominant; low-amp fast	Very low (atonia-like)	Twitches / minor moves	Autonomic variability↑; θ + atonia combo
Freezing (defensive)	Wake-like; sometimes θ↑	Moderate (rigid-not atonia)	Immobility with vigilance	Bradycardia; high vigilance
Absence seizure	7–12 Hz SWD (generalized)	Low–mod	Behavioural arrest; short bouts	SWD defines
PPN-induced global arrest	Onset-locked; γ↓; no δ build up	Low	Instant pause-and-play	Apnea + bradycardia (decisive)
Narcolepsy (incl. cataplexy)	REM-EEG (θ); rapid transitions	Very low during cataplexy	Emotion-triggered collapse; instability	Emotion trigger + REM-EEG + atonia
Catalepsy (neuroleptic-induced)	δ↑; δ–high-γ PAC↑ (M1) reports	Rigid (↑)	Immobility with waxy flexibility	Drug-induced; no REM-like EEG
General anesthesia (propofol)	δ↑ + frontal α–coherence	Very low	Unresponsive	Autonomic suppression; not upright

Entries labeled "This study" indicate states directly observed or defined in the present experiments (Interm-C, State-C). Other entries (e.g., REM, SWS, narcolepsy, catalepsy, anesthesia) are based on representative literature in mice[28-30].

Symbols vs Awake: ✓ prominently observed; ≈ no change; ↑ / ↓ increase / decrease; ↑↑ / ↓↓ marked change; ✕ absent.

Rodent frequency bands: δ = 0.5–4 Hz; θ = 6–9 Hz; γ = 30–80 Hz.

Measures are from mice; Interm-C and State-C entries derive from this study.

Abbreviations: SWD, spike-and-wave discharge (generalized 7–12 Hz paroxysms typical of rodent absence seizures); NREM, non-rapid eye movement sleep; HR, heart rate; PAC, phase–amplitude coupling (cross-frequency coupling quantified by the modulation index); PPN, pedunculopontine nucleus.

Extended Data Table 2 |
State-dependent neural and behavioural signatures.
(All measures are normalized to Awake)

Measure	**Awake (reference)**	**Interm-C**	**SWS**	**State-C**
Goal-directed behaviour	–	↓↓	×	×
Locomotion (gross motor output)	–	↓	×	×
EMG (arousal)	–	≈	↓	↓
EEG γ-power (30–80 Hz)	–	≈	↓	↓
EEG δ-power (0.5–4 Hz)	–	≈	↑↑	↑
Ca^{2+}/spiking rate (gross)	–	≈	↓	↓
Pairwise spike correlation	–	↓	↑*	↓
Dimensionality (D_{50})	–	↑	↓*	↑
Dimensionality (PR)	–	↑	↓*	↑

Behavioural tasks (Figs. 3–5), EMG/EEG (Extended Data Fig. 5), Ca^{2+} / spiking (Fig. 5e), pairwise correlation (Fig. 5f), and D_{50} and PR (Extended Data Fig. 8d,e).
Symbols: —, reference (Awake); ≈, no detectable change; ↓ / ↑, decrease / increase; ↑↑ / ↓↓, marked change; ×, not observed or not applicable; *, as reported previously (SWS shows increased correlations and reduced dimensionality)[33].
D_{50}, number of principal components explaining 50% of the variance; PR, participation ratio.
See Methods for frequency band definitions and statistics.

Summary:
Interm-C — γ ≈; pairwise correlation ↓; PR ↑.
State-C — spiking SWS-like; γ ↓; δ slight ↑; PR ↑.

Extended Data Movies are available at Figshare

(DOI:**https://doi.org/10.6084/m9.figshare.30338965**)

Extended Data Movie 1 | Laser-dot task (WT mouse)

A wild-type (z233) mouse wearing an EEG headset chased a laser dot projected onto the corner of a small open field (19.4 × 19.4 cm) within 10 s. The laser was directed toward the corner to avoid reflections, although mice normally chase the laser dot even on a flat surface. The movie is shown at 2× real time.

Extended Data Movie 2 | Laser-dot task (SynC@FPC mouse before i.p. A/C)

A SynC@FPC mouse (z244-5, 1117 s before A/C) expressing SynC broadly in the frontoparietal cortex chased the laser dot within 10 s, similarly to the WT mouse. The movie is shown at 2× real time.

Extended Data Movie 3 | Laser-dot task (SynC@FPC mouse after i.p. A/C)

The same SynC@FPC mouse (z244-5, 2298 s after A/C) as in Movie 2. The mouse failed to chase the laser dot within 10 s. The movie is shown at 2× real time.

Extended Data Movie 4 | Laser-dot task (SynC@FPC mouse 1 h after i.p. A/C)

The same SynC@FPC mouse (z244-5, 3483 s after A/C) as in Movie 2 and 3. The mouse again chased the laser dot within 10 s, indicating recovery of normal behaviour. The movie is shown at 2× real time.

Extended Data Movie 5 | Food-pellet task (WT mouse after i.p. A/C)

A WT mouse (z239, 785 s after A/C) grasped and ate a food pellet placed in the arena within 30 s. The movie is shown at 2× real time.

Extended Data Movie 6 | Food-pellet task (SynC@FPC mouse after i.p. A/C)

A SynC@FPC mouse (z227-6, 1203 s after A/C) repeatedly passed over the food pellet without eating, eventually beginning to consume it only after 5 min. The mouse spent an unusually long period grooming near the pellet and showed no response to the laser dot before finally grasping and eating the pellet. The movie is shown at 2× real time.

Extended Data Movie 7 | Food-pellet task (SynC@FPC mouse 1 h after i.p. A/C)

The same mouse (z227-6, 5204 s after A/C) as in Movie 6. The mouse rapidly approached, grasped, and ate the food pellet within 10 s. The movie is shown at 2× real time.

Extended Data Movie 8 | "Standing" posture example 1 during State-C (SynC@FPC mouse)

A SynC@FPC mouse (z156-3, 444 s after A/C) exhibited a "standing" posture upon behavioural arrest during running, shown from side and top views in a small (15 × 15 cm) open field. EEG, EMG, and velocity traces are displayed simultaneously. The movie is shown in real time.

Extended Data Movie 9 | "Standing" posture example 2 during State-C (SynC@FPC mouse)

A SynC@FPC mouse (z248-2, 1007 s after A/C) exhibited a "standing" posture upon behavioural arrest during running, shown from side and top views in a small (19.4 × 19.4 cm) open field. EEG, EMG, and velocity traces are displayed simultaneously. The movie is shown in real time.

Extended Data Movie 10 | "Grooming" posture during State-C (SynC@FPC mouse)

A SynC@FPC mouse (z248-1, 1873 s after A/C) exhibited a "grooming" posture upon behavioural arrest during grooming, shown from side and top views in a small open field. EEG, EMG, and velocity traces are displayed simultaneously. The movie is shown in real time.

Extended Data Movie 11 | "Corner" posture during State-C (SynC@FPC mouse)

A SynC@FPC mouse (z248-2, 1241 s after A/C) exhibited a "corner" posture upon behavioural arrest while approaching a corner in the small open field. EEG, EMG, and velocity traces are displayed simultaneously. The movie is shown in real time.

Extended Data Movie 12 | "Shifting" posture during State-C (SynC@FPC mouse)

A SynC@FPC mouse (z244-2) exhibited brief "shifting" movements at 115 s and 225 s following a corner posture, coinciding with short bouts (0.5 s and 2 s) of Interm-C. EEG, EMG, and velocity traces are displayed simultaneously. The movie is shown in real time.

Extended Data Movie 13 | Normal sleep-preparation behaviour (WT mouse)

Before sleep onset, a WT mouse (z155-2, 1198 s after A/C) slowly walked toward a corner as EEG γ-power was already decreasing. The mouse then turned to face the centre, curling its body and tail. EEG δ-power increased after the mouse adopted a full sleep posture. The movie is shown in real time.

Extended Data Movie 14 | Transition from Interm-C to State-C (SynC@FPC mouse)

A SynC@FPC mouse (z178-4, 1415 s after A/C) walked toward a corner and abruptly entered behavioural arrest precisely when EEG γ-power declined sharply. EEG δ-power showed only a slight increase. Spindle waves appeared shortly after the onset of State-C in this case. The movie is shown in real time.

Extended Data Movie 15 | Treadmill running before i.p. A/C (SynC@FPC mouse)

A mirror beneath the treadmill captured normal running and transient stalling movements of the SynC@FPC mouse (z251-3, 1478 s before A/C), whose hindlimbs were widely spaced, providing stable treadmill control. The movie is shown in real time.

Extended Data Movie 16 | Treadmill running after i.p. A/C (SynC@FPC mouse)

The same SynC@FPC mouse (z251-3, 614 s after A/C) as in Movie 15 showed somewhat clumsier running (hindlimbs narrowly spaced) and occasional stalling, failing to adequately control the treadmill. The movie is shown in real time.